

Molecular Gas in NUClei of GALaxies (NUGA)

I. The counter-rotating LINER NGC 4826*

S. García-Burillo¹, F. Combes², L. K. Hunt³, F. Boone⁴, A. J. Baker⁵, L. J. Tacconi⁵, A. Eckart⁶, R. Neri⁷, S. Leon⁸, E. Schinnerer⁹, and P. Englmaier¹⁰

¹ Observatorio Astronómico Nacional (OAN)-Observatorio de Madrid, Alfonso XII, 3, 28014-Madrid, Spain

e-mail: burillo@oan.es

² Observatoire de Paris, LERMA, 61 Av. de l'Observatoire, 75014-Paris, France

e-mail: francoise.combes@obspm.fr

³ Istituto di Radioastronomia/CNR, Sez. Firenze, Largo Enrico Fermi, 5, 50125-Firenze, Italy

e-mail: hunt@arcetri.astro.it

⁴ Astronomisches Institut der Ruhr-Universität Bochum, Universitätsstrasse 150, D-44780, Germany.

e-mail: fboone@astro.ruhr-uni-bochum.de

⁵ Max-Planck-Institut für extraterrestrische Physik, Postfach 1312, D-85741 Garching, Germany

e-mail: ajb@mpe.mpg.de, linda@mpe.mpg.de

⁶ Universität zu Köln, I. Physikalisches Institut, Zùlpicherstrasse 77, 50937-Köln, Germany

e-mail: eckart@ph1.uni-koeln.de

⁷ Institut de Radio-Astronomie Millimétrique (IRAM), 300 Rue de la Piscine, 38406-St.Mt.D'Hères, France

e-mail: neri@iram.fr

⁸ Instituto de Astrofísica de Andalucía (CSIC), C/ Bajo de Huétor, 24, Apartado 3004, 18080-Granada, Spain

e-mail: stephane@iaa.es

⁹ National Radio Astronomy Observatory, P.O. Box 0, Socorro, NM87801, USA

e-mail: eschinne@nrao.edu

¹⁰ Astronomisches Institut, Universität Basel, Venusstrasse 7, CH-4102, Binningen, Switzerland

e-mail: ppe@astro.unibas.ch France

Received February 7th, 2003; accepted —, 2003

Abstract. We present new high-resolution observations of the nucleus of the counter-rotating LINER NGC 4826, made in the $J=1-0$ and $J=2-1$ lines of ^{12}CO with the IRAM Plateau de Bure mm-interferometer (PdBI). The CO maps, which achieve $0.8''$ (16 pc) resolution in the 2–1 line, fully resolve an inner molecular gas disk which is truncated at an outer radius of 700 pc. The total molecular gas mass ($3.1 \times 10^8 M_{\odot}$) is distributed in a lopsided nuclear disk of 40 pc radius, containing 15% of the total gas mass, and two one-arm spirals, which develop at different radii in the disk. The distribution and kinematics of molecular gas in the inner 1 kpc of NGC 4826 show the prevalence of different types of $m=1$ perturbations in the gas. Although dominated by rotation, the gas kinematics are perturbed by streaming motions related to the $m=1$ instabilities. The non-circular motions associated with the *inner* $m=1$ perturbations (lopsided instability and inner one-arm spiral) agree qualitatively with the pattern expected for a trailing wave developed outside corotation ('fast' wave). In contrast, the streaming motions in the *outer* $m=1$ spiral are better explained by a 'slow' wave. A paradoxical consequence is that the inner $m=1$ perturbations would not favour AGN feeding. An independent confirmation that the AGN is not being generously fueled at present is found in the low values of the gravitational torques exerted by the stellar potential for $R < 530$ pc. The distribution of star formation in the disk of NGC 4826 is also strongly asymmetrical. The observed asymmetries, revealed by HST images of the inner disk, follow the scales of the various $m=1$ perturbations identified in the molecular gas disk. Massive star formation is still vigorous, fed by the significant molecular gas reservoir at $R < 700$ pc. There is supporting evidence for a recent large mass inflow episode in NGC 4826. The onset of $m=1$ instabilities of the type observed in NGC 4826 may be a consequence of secular evolution of disks with high gas mass contents.

These observations have been made in the context of the *NUclei of GALaxies* (NUGA) project, aimed at the study of the different mechanisms for gas fueling of Active Galactic Nuclei (AGN).

Key words. Galaxies:individual:NGC 4826 – Galaxies:ISM – Galaxies:kinematics and dynamics – Galaxies:nuclei – Galaxies:Seyfert – Radio lines:galaxies

1. Introduction

1.1. Feeding Active Galactic Nuclei: the Nuclei of Galaxies (NUGA) project

Although there is observational evidence that the majority of galaxies contain super-massive black holes in their nuclei, the existence of nuclear activity is far from universal (Ho et al. 1997). It is commonly accepted that nuclear activity results from the feeding of a massive black hole by the infall of gas from its host galaxy. However, there is no consensus on which mechanisms are responsible for removing the angular momentum from the gas and driving infall down to scales of tens of pc. Moreover, it is unknown whether these mechanisms are at work only in active galaxies, or, alternatively, if the key difference between active and quiescent objects is the availability of gas supply to the nucleus. On large scales, several dynamical perturbations induced by galaxy collisions, mergers and mass accretion (Heckman et al. 1986) can effectively drive infall of gas to scales of $\sim 1 - 3$ kpc. Numerical simulations have also shown that gravity torques from barred potentials are efficient at funneling gas into the center of a galaxy. Observational support for the role of bars in driving gas inflow at these scales has been found (Sakamoto et al. 1999). However, when an Inner Lindblad Resonance (ILR) is present, the gas accumulates in rings (Combes 1988; Piner et al. 1995; Buta & Combes 1996); subsequently there is virtually no gas infall to the nucleus, as gravity torques are positive inside the ILR.

To explain the mass transfer from the ~ 1 kpc scale to radii of tens of pc, we must deal with the non-trivial problem of angular momentum removal. Possible solutions have invoked the onset of non-axisymmetric dynamical perturbations such as nested nuclear bars (Shlosman et al. 1989; Friedli & Martinet 1993); lopsidedness or $m=1$ instabilities (Shu et al. 1990; Kormendy & Bender 1999; García-Burillo et al. 2000); warped nuclear disks (Pringle 1996; Schinnerer et al. 2000a, 2000b); and nuclear spiral density waves (Englmaier & Shlosman 2000).

The study of interstellar gas in the nuclei of galaxies is a fundamental tool for understanding nuclear activity and its relation to circumnuclear star formation. From the theoretical point of view, there is an increasing body of evidence that purely gaseous density waves (spirals, bars, warps or lopsided instabilities) may be driving gas infall to the Active Galactic Nucleus (AGN) (Heller & Shlosman 1994; Elmegreen et al. 1998; Regan & Mulchaey 1999). Within the central kiloparsec, most of the gas is in the molecular phase, which makes CO lines the best tracers of nuclear gas dynamics. Up to now, CO surveys of galaxies made with single-dish telescopes were hampered by insufficient spatial resolution (Kenney & Young 1988; Heckman et al. 1989; Young et al. 1995; Braine et al. 1993;

Casoli et al. 1996; Vila-Vilaro et al. 1998). Most CO interferometer surveys of nearby spirals (Sakamoto et al. 1999; Regan et al. 2001; Helfer et al. 2003) mapped CO(1-0) disk emission at low spatial resolution ($4''-7''$) and moderate sensitivity (detectability thresholds $\Sigma_{gas} > 180M_{\odot}/pc^2$). Furthermore, until very recently (Jogee et al. 2001), the published survey samples have included very few AGN.

A study of the gas fueling in AGN absolutely requires high ($\sim 0.5''-1''$) spatial resolution, given the small ($\sim 50-100$ pc) linear scales involved. We also need high sensitivity to provide a high dynamic range in the synthesized maps. The *Nuclei of Galaxies* project—NUGA—(García-Burillo et al. 2003) is a high-resolution, high-sensitivity CO survey of a sample of 12 nearby AGN which spans the sequence of activity types (Seyfert 1, Seyfert 2 and LINERs). The survey is being carried out with the IRAM Plateau de Bure mm-interferometer (PdBI) in France, which offers the best combination of sensitivity and resolution crucial for this project. NUGA aims at reaching spatial resolutions $< 1''$ and will allow the acquisition of CO maps with high dynamic ranges for most of the targets. Our objective is to determine the distribution and dynamics of molecular gas in the inner 1 kpc of the nuclei with resolutions of $\sim 10-50$ pc, and to study systematically the different mechanisms for gas fueling of the AGN.

The NUGA project relies on a multi-wavelength approach: the sample of galaxies observed at PdBI has been defined based on the availability of high-quality optical and near-infrared (NIR) images. These images have been obtained with both ground-based telescopes and the Hubble Space Telescope (HST). The optical and NIR counterpart of NUGA will provide the stellar potentials, the star formation history and the dust distributions for the galaxies in our sample. We will thus be able to study quantitatively the debated AGN-starburst connection. NIR maps will be used to compute the stellar potentials. These will be the basis for self-consistent numerical simulations of the gas dynamics (obtained from CO) in real case scenarios (defined by the optical and NIR images). The long term aim is to complete a super-sample of 25-30 objects observed by consortium members, within and outside NUGA, with the IRAM array. The initial papers will exploit on a case-by-case basis the data obtained in the context of the NUGA project.

1.2. The counter-rotator LINER NGC 4826

In this first paper, we study the distribution and dynamics of molecular gas in the nucleus of the LINER NGC 4826, using high-resolution ($0.8''-3''$) observations made in the 1-0 and 2-1 lines of ^{12}CO with the IRAM array. NGC 4826, also known as the 'Black Eye' or 'Evil Eye galaxy' due to its optical appearance, hosts two nested counter-rotating gas disks of comparable mass. The inner disk extends to a radius of $\sim 50''$ and contains $\sim 10^7 M_{\odot}$ of atomic (HI) gas (Braun et al. 1992, 1994) and $\sim 2.3 \times 10^8 M_{\odot}$ of molecular (H_2) gas (Casoli & Gerin

Send offprint requests to: S.García-Burillo

* Based on observations carried out with the IRAM Plateau de Bure Interferometer. IRAM is supported by INSU/CNRS (France), MPG (Germany) and IGN (Spain)

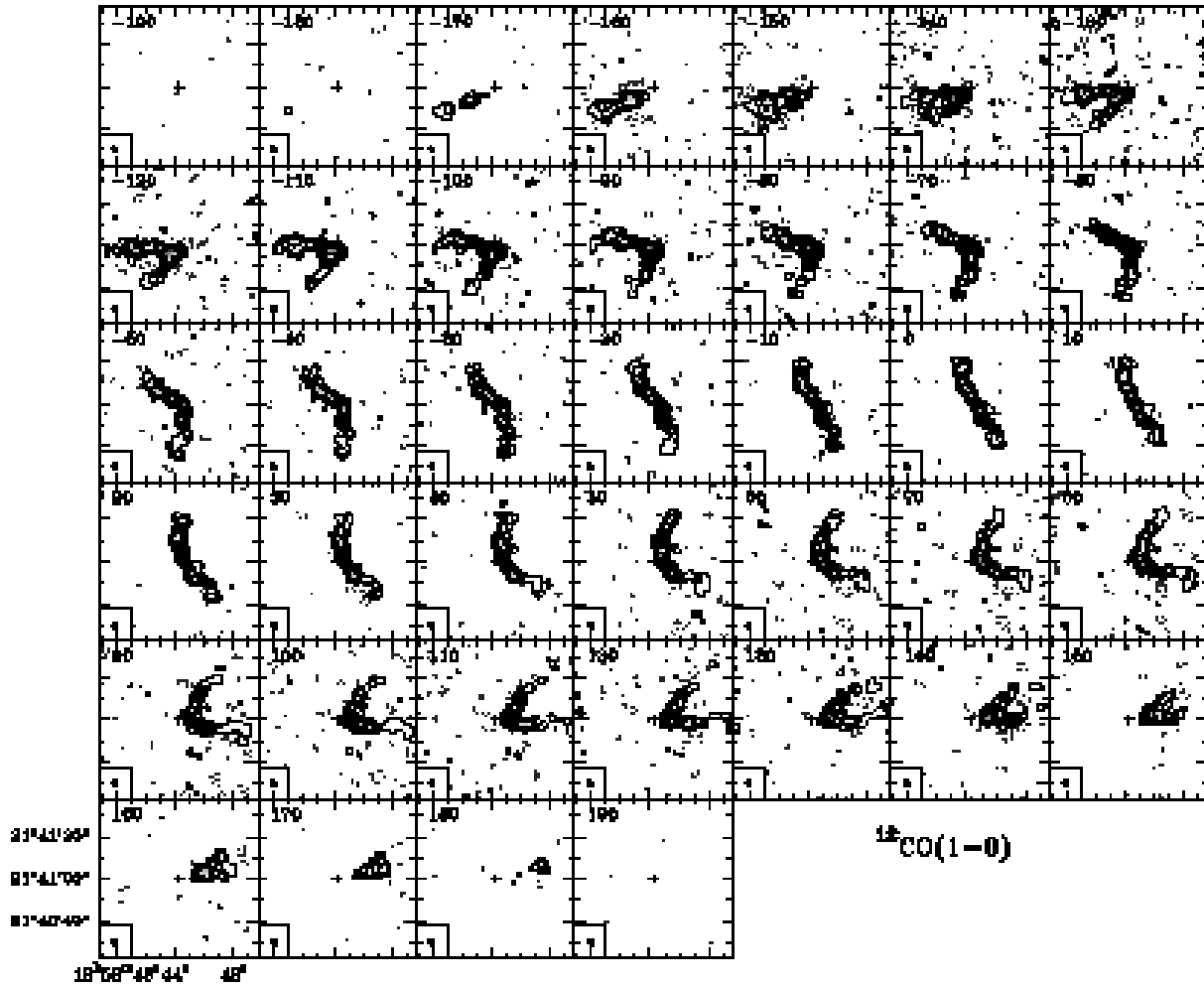


Fig. 1. $^{12}\text{CO}(1-0)$ velocity-channel maps observed with the PdBI in the nucleus of NGC 4826 with a spatial resolution of $3'' \times 2.4''$ at $\text{PA}=44^\circ$ (beam is plotted as a filled ellipse in the bottom left corner of each panel). We show a field of view of $75''$, i.e. ~ 1.8 times the diameter of the primary beam at 115 GHz. The phase tracking center is indicated by a cross at $\alpha_{J2000}=12^{\text{h}}56^{\text{m}}43.88^{\text{s}}$ and $\delta_{J2000}=21^\circ 41' 00.1''$. Velocity-channels are displayed from $v=-190 \text{ km s}^{-1}$ to $v=190 \text{ km s}^{-1}$ in steps of 10 km s^{-1} . Velocities are in LSR scale and referred to $v=v_o=408 \text{ km s}^{-1}$. Contour levels are -3σ , 3σ , 10σ , 20σ , 40σ and 78σ where the 1-sigma rms $\sigma=4.0 \text{ mJy beam}^{-1}$. There are very few pixels with negative fluxes below -3σ inside the field-of-view.

1993). The outer disk, extending from $\sim 80''$ to $\sim 9.8'$, rotates in the opposite sense to the inner gas and contains $\sim 10^8 M_\odot$ of HI (Braun et al. 1992, 1994). Rix et al. (1995), by studying the stellar kinematics along the principal axes of NGC 4826, found that the stars rotate at all radii with the same sense as the inner disk providing strong evidence that stars and gas are coplanar. However, the kinematics of the ionized gas, analyzed by Rubin (1994) and Rix et al. (1995), are considerably more complex. Within radii $< 30''$, ionized gas co-rotates with HI and the stars, followed by a strong kinematic disturbance in the region $30'' < r < 100''$, where rotation velocity is close to zero. Most remarkably, Rix et al. (1995) found evidence for radial inflow along the minor axis.

Casoli & Gerin (1993) made low-resolution $^{12}\text{CO}(1-0)$ ($22''$) and $^{12}\text{CO}(2-1)$ ($12''$) maps of NGC 4826's disk using the IRAM 30m telescope. Their maps showed that the co-rotating molecular disk ends quite abruptly at a

radius of $45-50''$, i.e., at a significantly small extent relative to the optical galaxy size ($D_{25}=10'$). These low-resolution maps could not reveal the small-scale structure and kinematics of the compact molecular disk. NGC 4826 was also observed as a part of the interferometer surveys of OVRO (Sakamoto et al. 1999) and BIMA-SONG (Helfer et al 2003). These interferometer maps confirmed that the molecular gas disk of NGC 4826 extends out to a radius of 700 pc. The OVRO map of NGC 4826, published by Sakamoto et al. (1999), shows tantalizing evidence of an asymmetrical distribution of molecular gas in the inner 1 kpc.

The maps presented in this paper fully resolve the molecular gas distribution in NGC 4826 out to a radius of $r=35''$ (700 pc). The high spatial resolution ($0.8''=16 \text{ pc}$ in the 2-1 line) and high dynamic range ($\sim 70-100$) of these observations allow the study of the complex pattern of gravitational instabilities at work from 1 kpc to

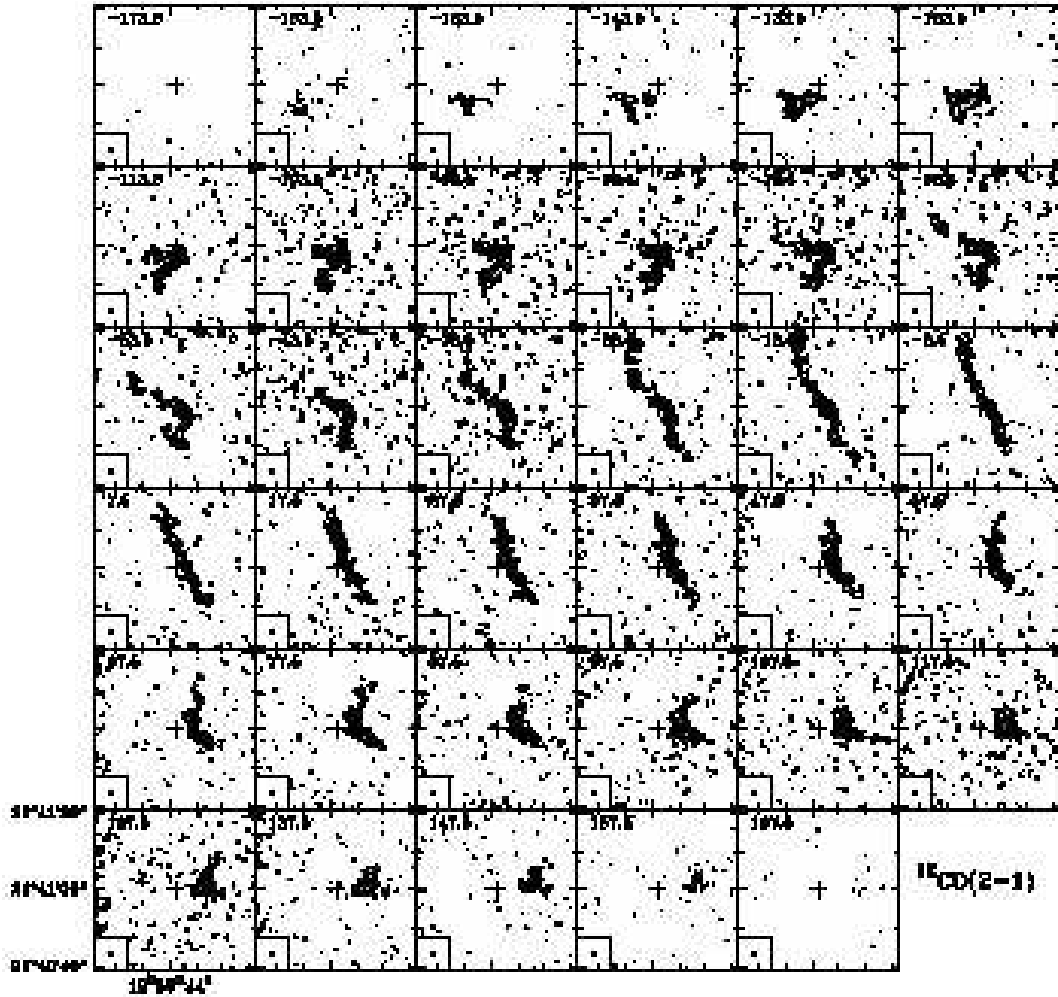


Fig. 2. Same as **Fig. 1** but for the 2–1 line of ^{12}CO . Spatial resolution reaches $1.1'' \times 0.8''$ at $\text{PA}=34^\circ$ (beam is plotted as a filled ellipse in the bottom left corner of each panel). We show a field of view of $43''$, i.e. ~ 2 times the diameter of the the primary beam at 230 GHz. Velocity-channels are displayed from $v=-172.5 \text{ km s}^{-1}$ to $v=167.5 \text{ km s}^{-1}$ in steps of 10 km s^{-1} , with same reference as used in **Fig. 1**. Contour levels are -4σ , 4σ , 8σ , 16σ , 32σ and 62σ , where the 1-sigma rms $\sigma=5.7 \text{ mJy beam}^{-1}$. There are very few pixels with negative fluxes below -4σ inside the field-of-view.

10-20 pc scales. Particular attention is devoted to exploring the influence that counter-rotating instabilities may have in driving gas inflow. We also compare in detail the CO maps with other gaseous/stellar tracers in order to obtain a global picture of the gas response to the stellar potential in NGC 4826. Finally, we study the distribution of star formation in the nucleus, using HST archive broadband and narrow-band images.

2. Observations

2.1. CO observations

Observations of the nuclear region of NGC 4826 were carried out with the IRAM interferometer between December 2000 and January 2002, using the BCD set of config-

urations of the array (Guilloteau et al. 1992). We observed simultaneously the $J=1-0$ and $J=2-1$ lines of ^{12}CO in a single field centered at $\alpha_{J2000}=12^{\text{h}}56^{\text{m}}43.88^{\text{s}}$ and $\delta_{J2000}=21^\circ 41' 00.1''$; the primary beam size is $42''$ ($21''$) in the 1–0 (2–1) line. The spectral correlator was split in two halves centered at 115.114 GHz and 230.224 GHz, respectively, i.e., the transition rest frequencies corrected for an assumed recession velocity of $v_o(\text{LSR})=408 \text{ km s}^{-1}$. The correlator configuration covers a bandwidth of 580 MHz for each line, using four 160 MHz-wide units; this is equivalent to 1510 km s^{-1} (755 km s^{-1}) at 115 GHz (230 GHz). The correlator was regularly calibrated by a noise source inserted in the IF system. Visibilities were obtained using on-source integration times of 20 minutes framed by short ($\sim 2 \text{ min}$) phase and amplitude calibrations on the nearby quasars 1308+326 and 3C273. The data were phase cali-

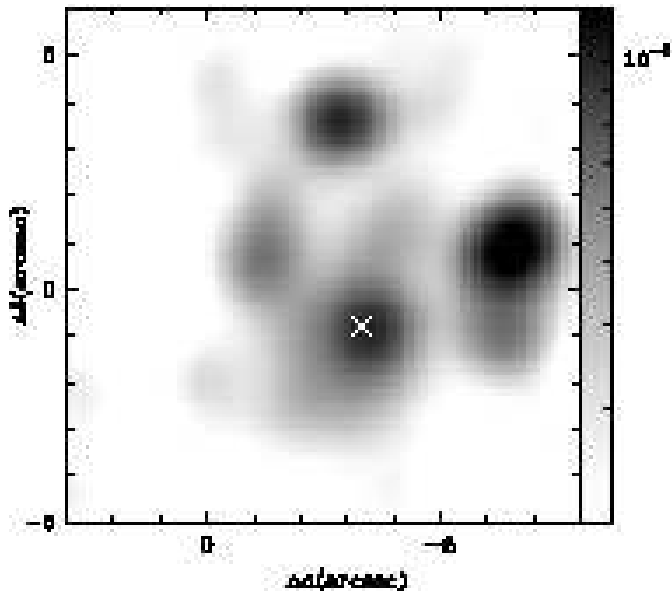


Fig. 3. The VLA radio-continuum map at 6 cm from Turner and Ho (1994), in grey logarithmic scale from 0.2 to 12 mJy beam⁻¹. We highlight the position of the dynamical center derived from CO (star marker) which coincides with a strong non-thermal source.

brated in the antenna-based mode. The flux of the primary calibrators was determined from IRAM measurements and taken as an input to derive the absolute flux density scale in our map; the latter is estimated to be accurate to 10%. The bandpass calibration was carried out using 3C273 and is accurate to better than 5%.

The point source sensitivities derived from emission-free channels of 10 km s⁻¹ width are 4.0 mJy beam⁻¹ in ¹²CO(1-0) and 5.7 mJy beam⁻¹ in ¹²CO(2-1). The image reconstruction was done using standard IRAM/GAG software (Guilloteau & Lucas 2000). Unless explicitly stated, we used natural weighting and no taper to generate the 1-0 line maps with a field of view of 75'' and 0.25'' sampling; the corresponding synthesized beam is 3.0'' × 2.3'', PA=44°. We used uniform weighting to generate 2-1 maps with a field of view of 43'' and 0.20'' sampling; this enables us to achieve a spatial resolution <1'' (1.1'' × 0.8'', PA=34°). No 3mm (1mm) continuum was detected towards NGC 4826, down to an rms noise level of 0.38 mJy beam⁻¹ (0.67 mJy beam⁻¹) in a 564 MHz-wide band centered on 113.6 GHz (231.7 GHz). The conversion factors between Jy beam⁻¹ and K are 13 K Jy⁻¹ beam at 115 GHz, and 25 K Jy⁻¹ beam at 230 GHz. By default, all velocities are referred to v_o and (Δα, Δδ) offsets are relative to the phase tracking center. Except for channel maps, all displayed maps are corrected for primary beam attenuation. We will assume a distance to NGC 4826 of D=4.1 × (75 H_o⁻¹) Mpc (Tully 1988); H_o = 75 km s⁻¹ Mpc⁻¹ implies 1''=20 pc. We will assume that the inclination angle of NGC 4826's disk is i=60° (Rubin 1994); we derive here a position angle of

PA=112±8°, in rough agreement with previous determinations (e.g., PA=120±5°; Rix et al. 1995).

2.2. Optical and near-infrared observations

We acquired from the HST archive three broad-band images of NGC 4826, including WFPC2 (F450W (~ B band) and F814W (~ I band)) and NICMOS (NIC3: F160W (~ H band)); we also obtained a Paα image (F187N) as this galaxy was included in the survey of Böker et al. (1999). The optical images were combined with elimination of cosmic rays (*erreject*), and calibrated as described in Holtzman et al. (1995). Sky values were assumed to be zero. This was checked to be in general a good assumption with related NICMOS data (Hunt & Malkan 2003 in prep), and gives H-band magnitudes that agree to within 0.1 mag with ground-based data. The NICMOS images were re-reduced using the best calibration files and the van der Marel algorithm was used to remove the “pedestal” effect (see Böker et al. 1999). The continuum was subtracted from the Paα image according to the precepts explained in Böker et al. (1999), but only for the brightest pixel values (we excluded roughly half the pixels in the image). It was necessary to adjust the slope of F160W-F187N such that the nucleus remained > 0 everywhere (see also García-Burillo et al. 2000). The fields-of-view are 2.7' × 2.7' and 51'' × 51'', respectively, for the WFPC2 and NICMOS images.

Optical and near-infrared surface-brightness profiles of NGC 4826 were measured along the minor axis (PA = 22°) with a 3'' width, and used to derive color profiles after rebinning to a 0.1'' pixel scale. These will be discussed in Sect. 4.

3. Results

3.1. Position of the AGN

Fig. 1-2 show the velocity-channel maps of ¹²CO(1-0) and ¹²CO(2-1) emission in the central region of NGC 4826. The typical spider web diagram visible in the maps is the signature of a spatially resolved rotating disk. The eastern (western) side of the CO disk is blue (red)-shifted with respect to the reference velocity v_o. The velocity field indicates that molecular gas co-rotates with the stars (Rix et al. 1995) and the HI gas (Braun et al. 1992) to a radius of 700 pc. We find no evidence of counter-rotating molecular gas in the inner disk. The best fits for the center of rotation and systemic velocity are (Δα, Δδ) = (-3.3'', -0.8'') and v_{sys}^{LSR} = v_o + 8 km s⁻¹ = 416 km s⁻¹, respectively. Within the errors, the derived dynamical center coincides with the position where CO lines reach their maximum widths (~150–200 km s⁻¹). The CO dynamical center lies very close (±0.2'') to a strong non-thermal continuum source present in the 6cm map of Turner & Ho (1994) (their source number 5; see also Fig. 3 in this work). Furthermore, the dynamical center coincides, within the errors, with the position of

a X-ray source detected in the high-resolution ($0.5''$) CHANDRA image of the nucleus of NGC 4826 (source S3; PI:Gordon Garmire, id. 411). Therefore, we ascribe the position $\alpha_{J2000} = 12^{\text{h}}56^{\text{m}}43.64^{\text{s}}$, $\delta_{J2000} = 21^{\circ}40'59.3''$ to both the dynamical center and the LINER nucleus in NGC 4826. The systemic velocity derived from CO [$v_{\text{sys}}(\text{LSR})=416\pm 5 \text{ km s}^{-1}=v_{\text{sys}}(\text{HEL})=408\pm 5 \text{ km s}^{-1}$] agrees satisfactorily with the value determined from HI [$v_{\text{sys}}(\text{HEL})=408\pm 8 \text{ km s}^{-1}$ from RC3].

3.2. The NGC 4826's molecular gas disk

3.2.1. Molecular gas masses

The velocity-integrated $^{12}\text{CO}(1-0)$ flux within the $42''$ primary beam field corrected for primary beam attenuation is $S_{\text{CO}}=1.58\times 10^3 \text{ Jy km s}^{-1}$. Assuming a CO-to- H_2 conversion factor $X=\text{N}(\text{H}_2)/\text{I}_{\text{CO}}=2.2\times 10^{20} \text{ cm}^{-2} \text{ K}^{-1} \text{ km}^{-1} \text{ s}$ (Solomon & Barrett 1991), the total H_2 mass derived from the interferometer map is $M(\text{H}_2)=2.3\times 10^8 M_{\odot}$. Including the mass of helium, the total molecular gas mass in the $^{12}\text{CO}(1-0)$ Bure field is $M_{\text{gas}}=M(\text{H}_2+\text{He})=1.36\times M(\text{H}_2)=3.1\times 10^8 M_{\odot}$, in good agreement with the estimate of $3\times 10^8 M_{\odot}$ by Sakamoto et al. (1999). We estimate that the PdBI map recovers close to 100% of the single-dish $^{12}\text{CO}(1-0)$ flux measured by Casoli & Gerin (1993) with the IRAM 30m.

The overall distribution of molecular gas is best seen in Fig. 4, which shows the velocity-integrated intensity ^{12}CO maps. These were derived by integrating channels from $v = -200$ to 200 km s^{-1} . Although the $^{12}\text{CO}(1-0)$ map probably lacks the sensitivity to detect gas emission beyond $r\sim 35''$, we find little evidence that NGC 4826's molecular disk extends significantly outside the $42''$ primary beam (see Fig. 1). This confirms the finding of Casoli & Gerin (1993) (see also Sakamoto et al. 1999) who reported that molecular gas is confined to the inner 1.6 kpc of NGC 4826. While our $^{12}\text{CO}(2-1)$ map lacks sensitivity outside the central 500 pc of the disk, it gives a sharp image of the molecular gas distribution in the vicinity of the AGN (Fig. 4b).

3.2.2. The imprint of $m=1$ perturbations in the central kiloparsec of NGC 4826

Nearly $\sim 15\%$ of the total molecular gas mass is located in a circumnuclear disk (hereafter CND) around the AGN ($M_{\text{gas}}^{\text{CND}}=3.4\times 10^7 M_{\odot}$). This disk has a ~ 80 pc average radius and its boundaries are here defined by the eighth intensity contour of Fig. 4a. The small scale structure of the CND is fully resolved in the 2–1 map (Fig. 4b). At scales of \sim tens of pc, the CND has a lopsided morphology: there is a pronounced 20–60 pc offset between the AGN locus and a ridge of $^{12}\text{CO}(2-1)$ emission which roughly extends from the NE ($-3''$, $0.5''$) to the W side ($-6.5''$, $1''$) of the CND (see Fig. 4b). A similar offset between the center of NGC 4826 and the centroid of dense molecular gas was identified by Helfer & Blitz (1997). Their HCN(1–0) map

revealed a strong emission peak at $\sim(-1.5'', -1.5'')$, i.e., close to the ridge seen in $^{12}\text{CO}(2-1)$, offering supporting evidence that the distribution of molecular gas in the inner region of the CND ($R<60$ pc) is strongly lopsided. In the outer boundary of the CND ($R\sim 60-80$ pc) two weak winding spiral arcs can be tentatively identified in the 2–1 map, suggesting that secondary perturbations are at play.

Outside the CND, molecular gas emission is also detected along two spiral arms which are located at noticeably different radii in the disk. This indicates that also at these scales (100–700 pc) the distribution of molecular gas is asymmetrical. An *inner* spiral arm (hereafter Arm I), identified in both the 1–0 and the 2–1 maps (Fig. 4), extends south of the CND. The CND and Arm I join at $\sim(2.5'', -3'')$. An *outer* spiral arm (hereafter Arm II), visible in the 1–0 map (Fig. 4a), extends north of the CND, starting from the western side of the disk [$\sim(-10'', 5'')$]. Arm II ends apparently on the SE side of the disk [at $\sim(22'', -15'')$]. However, CO emission is detected southward of the CND at declination offsets $\sim -20''$ with a significant 10σ level. Together with Arm II, this S arc would delineate an off-centered ring.

To highlight the geometry of Arms I and II, we have constructed the $^{12}\text{CO}(1-0)$ and $^{12}\text{CO}(2-1)$ peak brightness intensity maps (sensitive to contrasted structures) and deprojected them into the plane of the galaxy. Results are displayed in Fig. 5, which represent the deprojected brightness maps in polar grid coordinates [$\text{Log}_e(r), \Phi$]. Variable r is the galaxy deprojected radius in $''$ and Φ is the azimuthal angle in degrees (see Fig. 5 for details). In this representation, a spiral logarithmic feature would appear as a straight line with a non-zero slope.

As shown in Fig. 5, Arm I develops between $2.4<\text{Log}_e(r)<2.8$ ($11''<r<16''$) and $160^\circ<\Phi<280^\circ$. Arm I shows *only* a $2\times\pi$ -periodicity along Φ . In contrast to two-arm ($m=2$) spiral arms, one-arm ($m=1$) spirals are not π -periodic in azimuth. We can derive an average pitch angle (p) of the spiral from $\tan(p)=-\Delta\text{Log}_e(r)/\Delta\Phi$ along the arm; p is the angle between the spiral and a circle at a given radius, measured counter-clockwise. This gives $p\sim 167^\circ$ for Arm I. The dust lane seen in optical images of NGC 4826 is a projected foreground layer situated on the northern side of the galaxy, identifying this as the nearer side. According to the observed sense of rotation of the gas, we therefore conclude that Arm I is *trailing* with respect to the gas and the stellar flows. Interestingly, this is in agreement with the morphological analysis by Walterbos et al. (1994), who also deduced that the inner spiral structure must be trailing inside $R\sim 2.7$ kpc.

Arm II is seen in the outer disk in the range $2.8<\text{Log}_e(r)<3.5$ ($16''<r<33''$) and $65^\circ<\Phi<190^\circ$. Arm II shows a low order $2\times\pi$ -periodicity along Φ , characteristic of $m=1$ instabilities. A similar analysis as done for Arm I indicates that the pitch angle of Arm II changes midway from $p\sim 146^\circ$ (trailing) to $p\sim 10^\circ$ (leading). This sudden change of orientation might suggest that at this location ($R\sim 600$ pc) two spiral-like perturbations are meeting in the disk.

In summary, the distribution of molecular gas in the inner 1 kpc of NGC 4826 shows the prevalence of different types of asymmetrical $m=1$ perturbations in the gas disk. Besides two one-arm trailing spirals—Arms I and II—which develop in the outer region (radii ~ 100 – 700 pc), we have detected a lopsided CND. This indicates that $m=1$ perturbations extend to radial distances as small as ~ 20 – 60 pc from the AGN. As shown below, the gas kinematics in the inner 1 kpc reveal the presence of non-circular motions which are related to the various detected $m=1$ perturbations. A detailed analysis of these is developed in Sect. 3.3.2 to give an insight into the origin of $m=1$ perturbations in NGC 4826.

3.3. Kinematics of NGC 4826's molecular gas disk

3.3.1. The rotation curve and the dynamical mass

We show in Fig. 6 the mean velocity field maps obtained from the $^{12}\text{CO}(1-0)$ and $^{12}\text{CO}(2-1)$ data in the nucleus of NGC 4826 (derived with $2\text{-}\sigma$ clipping). The kinematics of molecular gas at radii $R < 700$ pc are consistent with those of a disk in direct rotation with respect to the stars.

A CO rotation curve (v_{rot}) has been derived from position-velocity (p-v) diagrams taken along the kinematic major axis of NGC 4826 (Fig. 7). We identify the major axis position angle as $\text{PA} = 112 \pm 8^\circ$; this value yields a larger line-of-sight velocity gradient within $R = 700$ pc than does a p-v cut through the dynamical center at any other angle. Our determination roughly agrees with previous findings based on H α and stellar kinematics ($\text{PA} = 120 \pm 5^\circ$; Rix et al 1995). We have calculated the terminal velocities, and from these, the rotation curve, by fitting gaussian profiles to the spectra across the major axis. The velocity centroids, corrected for inclination $i = 60^\circ$, give v_{rot} for each offset along the major axis. Rotation curves derived from both sides of the major axis do not differ significantly within the errors. Therefore, we have derived v_{rot} as a function of radius by averaging values from the W and E sides of the major axis. Data for both lines were noise-weighted averaged using a radial beaming of $\Delta r = 0.5''$.

The resultant v_{rot} (Fig. 8) shows a steep increase to the edge of the CND ($R \sim 70$ – 80 pc), where $v_{rot} \sim 120$ – 125 km s $^{-1}$. This trend is followed by a gradual increase up to a radius of $R \sim 350$ pc, after which v_{rot} remains flat at ~ 190 km s $^{-1}$. The rotation velocity of molecular gas follows the stellar and the ionized gas motions inside $R \sim 700$ pc (see Fig. 3 and 6 of Rix et al 1995).

The total mass inside the CND can be inferred using $M(R) = C \times R \times v_{rot}^2 / G$, where G is the constant of gravitation, $M(R)$ is the mass inside a sphere of radius R , and C is constant varying between 0.6 and 1, depending on the disk mass model assumed (Lequeux 1983). If we take a value of $C = 0.8$ intermediate between the values appropriate for spherical (1) and flat disk (0.6) distributions, $M(R = 70 \text{ pc}) \sim 2.3 \times 10^8 M_\odot$. This implies that the molecular gas mass fraction inside the CND is $\sim 15\%$, decreasing to $\sim 5\%$ within $R = 700$ pc.

With the value estimated for the rotation curve at a radius $R \sim 10$ pc ($v_{rot} \sim 58$ km s $^{-1}$) we can set an upper limit of $\sim 8 \times 10^6 M_\odot$ for the mass of the putative super-massive black hole in the nucleus of NGC 4826.

3.3.2. Streaming motions and $m=1$ modes

Although mainly characterized by circular rotation, the gas kinematics are perturbed by streaming motions. Isovelocities in Fig. 6 display a wavy pattern at the passage of both Arms I and II. Deviations from circular motion can be identified in Arm I as a systematic kink in the isovelocities which appear redshifted; as expected, the shift is most pronounced near the crossing of the galaxy minor axis where only radial motions have non-zero projection (see Fig. 9). We find a gradient across the minor axis from redshifted velocities in Arm I to blueshifted velocities in the adjacent interarm region located at larger radii (see Fig. 6a and Fig. 9). Deprojected into the galaxy plane, the radial velocities measured on Arm I indicate local outflow motions. In contrast, non-circular motions along Arm II indicate that gas velocities are systematically redshifted, a local signature of inflow motions (Fig. 6).

Departures from pure rotation, related to the lopsided instability, also characterize the CND kinematics. The average gas velocities derived from 2–1 data seem slightly redshifted (blueshifted) on the southern (northern) crossing of the lopsided feature along the minor axis (Fig. 9). Similarly to Arm I, these motions can be interpreted as a local signature of outflow. However radial streaming motions are neatly reversed in the outer boundary of the CND ($R \sim 60$ – 80 pc) where two secondary winding spiral arcs are identified in the 2–1 map (see Fig. 9).

The signatures of the streaming motions expected for trailing/leading waves can be analyzed in the framework of the linear density wave theory (Shu et al. 1973). The sign of velocity perturbations changes close to the minor axis when crossing from inside to outside the corotation resonance. A comparison with models may give some insight into the nature of the density waves that may account for the streaming motions observed in CO. García-Burillo et al. (2000) applied the general formalism to the case of one-arm ($m=1$) spirals for two extreme values of the pattern speed (Ω_p) illustrating the slow and the fast mode solutions. In the slow (fast) solution we are mostly inside (outside) corotation of the modes. In the case of NGC 4826, we have explored a fast solution by adopting a pattern speed large enough to assure corotation lies well inside the disk of the 'model' galaxy ($\Omega_p = 800$ km s $^{-1}$ kpc $^{-1}$); this implies $R_{COR} = 200$ pc for a rotation curve similar to v_{rot} . In contrast, a slow mode is here characterized by $\Omega_p = 0$ km s $^{-1}$ kpc $^{-1}$, i.e., a stationary wave where corotation is pushed outside the disk.

We represent in Fig. 10 the radial velocity perturbations, projected into the plane of the sky (v_{pert}), for the fast and slow one-arm trailing solutions. We purposely chose a disk geometry and spiral parameters qualitatively

similar to those of NGC 4826, apart from a lower inclination angle adopted here to give a more detailed picture of the velocity field in the model. Moreover, we can reasonably assume that the gas response (peak gas density) is close to the spiral potential minima in all cases. A comparison of the two model solutions with the CO observations indicates that the streaming motions measured on Arm I and, also, on the inner lopsided instability of the CND match qualitatively the solution of the fast trailing $m=1$ mode (Fig. 10): when the spiral arm is outside corotation, velocities are redshifted (blueshifted) on the southern (northern) side of the galaxy minor axis. In contrast, Arm II better matches the solution of the slow trailing mode (Fig. 10).

A paradoxical consequence is that the inner $m=1$ perturbations, represented by Arm I and the lopsided CND instability, would not favor gas infall: behaving as fast modes, the gas would gain angular momentum from the waves and would migrate outwards. In particular the AGN fueling might be temporarily blocked upon the onset of the inner lopsided instability. The perturbations identified in the outer boundary of the CND would favor gas inflow, however. This suggests that inflow and outflow may be globally counterbalanced in the CND. It remains to be determined, however, if angular momentum removal/gain from these instabilities, either stellar or gaseous, can be efficient enough to play some role in AGN feeding (see Sect. 6).

3.4. CO line ratios

To probe the physical conditions of the molecular gas in NGC 4826, we have studied the variation of the $^{12}\text{CO}(2-1)/^{12}\text{CO}(1-0)$ ratio in areas with significant emission levels in both lines (brightness temperatures $>5\sigma$). The 2–1 map was first degraded to the spatial resolution of the 1–0 map within the $21''$ primary beam to assure that the two lines sample identical regions; both maps were also corrected for primary beam attenuation.

The derived $^{12}\text{CO}(2-1)/^{12}\text{CO}(1-0)$ ratio is roughly constant over most of the disk, with a mean value 0.65 ± 0.05 . This ratio is close to the canonical value observed in other spiral disks and is typical of moderately dense optically thick molecular clouds (see García-Burillo et al. 1993). The only exception to this is in the vicinity of the AGN ($R < 50\text{--}100\text{ pc}$), where the measured ratio is close to 1. The highest values (~ 1.1) are observed toward the lopsided structure in the CND which coincides with the peak of emission detected in HCN (Helfer & Blitz 1997). Ratios are close to 0.8–0.9 in the strongest clumps along the spiral ridge of Arm I.

4. Star formation in NGC 4826

4.1. Distribution of star formation

The distribution of star formation in NGC 4826’s disk is strongly asymmetrical, as seen in the HST Pa α image

(see Fig. 11). The asymmetries follow with similar spatial scales the various $m=1$ instabilities identified in the CO maps. Interestingly, the overall star formation pattern shows a strong N/S asymmetry. While the $^{12}\text{CO}(1-0)$ emission on Arm II is associated with a strong ionized gas emission, to the southern far side in Arm I, where extinction is smaller, Pa α is significantly weaker. This is contrary to what would be expected if the reported N/S asymmetry was due mainly to heavy extinction by the conspicuous northern dust lane. Furthermore, the star formation pattern is also very asymmetrical in the CND (Fig. 11). We illustrate this in Fig. 12, which compares the Pa α morphology with the mostly thermal radio continuum emission at 2cm in the nucleus of NGC 4826 (from Turner & Ho 1994). A strong maximum is visible in both maps, which indicates that the star formation peaks neither on the AGN nor on the lopsided instability seen in the $^{12}\text{CO}(2-1)$ map, but rather 20 pc northward.

4.2. Extinction in the “Evil Eye”

The conspicuous dust lane identified in the optical pictures of NGC 4826 is expected to significantly screen any emission to the N. With the assumption of intrinsic axisymmetry for the stellar disk/bulge, Witt et al. (1994) determined the optical depth in the “Evil Eye”. Following Witt et al. (1994), we have re-examined the issue of extinction by extracting surface brightness profiles along the minor axis in F450W, F814W, and F160W. The relationship of this “cut” to the galaxy morphology is shown in Fig. 13; the profiles, averaged over $3''$ perpendicular to the direction of the cut, are shown in Fig. 13. The figure shows clearly the effects of extinction towards positive (northern) radii, and confirms the assumption that the stellar populations in the disk of NGC 4826 are rather symmetric, as the discrepancy between the northern and southern halves of the surface brightness profiles decreases substantially with increasing wavelength. However, the ionized gas emission is clearly intrinsically asymmetric since it is more prominent on the near side where there is more extinction.

We have derived the extinction map using the mean colors of the disk, as determined from the outer region of the cuts, toward the S, where (broadband) extinction is low or zero (see Witt et al. 1994). The $B-I$ mean color of the outer (S) region is 1.62, similar to, although 0.16 mag bluer than, the equivalent color from de Jong (1996) for integrated colors of similar morphological types. With the extinction coefficients given in Holtzman et al. (1995) for the WFPC2 filters, we then derived the extinction from the $B-I$ map. The mean extinction measured in the dust lane turns out to be not greater than $A_V = 1.5\text{ mag}$, in agreement with the findings of Waltherbos et al. (1994) and Witt et al. (1994). This confirms that the Pa α image of NGC 4826 is virtually extinction-free, and can be considered as a fair unbiased picture of how recent star formation proceeds in the central kpc of NGC 4826.

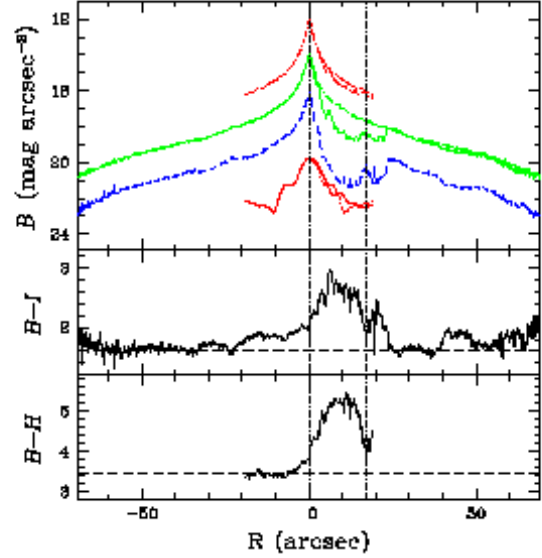
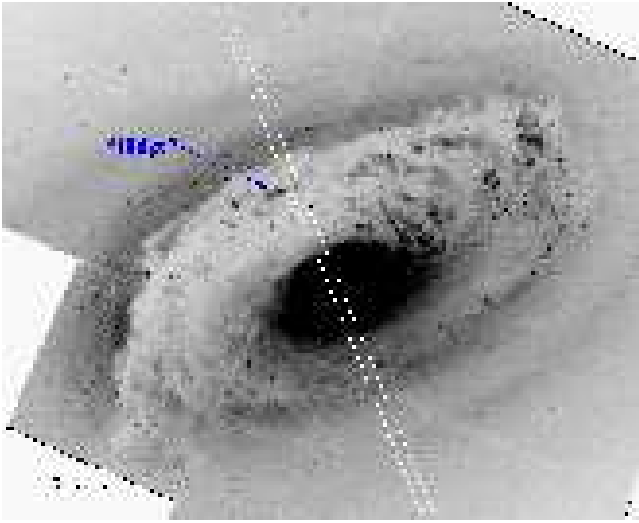


Fig. 13. a)(left) The F450W image of the galaxy with the “cut” aperture superposed. The brightness peak is shown with a cross in the black (brightest) central region, while a bright HII region is marked with a cross at a radial distance of 17''. **b)(right)** The surface brightness profile along the minor axis, together with the F450W–F814W $\sim B - I$ and F450W–F160W $\sim B - H$ colors. The center and HII region at $r \sim 17''$ shown by crosses in **a)(left)** are denoted here by vertical dotted lines. The F160W profile is shown by a dotted line, F814W by a solid line, F450W by a dashed line, and CO(1-0) by a heavy line (from top to bottom). Y axis units are magnitudes for all profiles, ‘including’ CO (in logarithmic scale with an arbitrary offset). In the top panel (for all curves except that for F450W), we plot the reflection of the southern half of the surface brightness profile underneath the northern half of the profile, showing the asymmetry induced by the dust lane. The horizontal dashed lines in the lower panels show the intrinsic color as estimated from the southern region, i.e., at negative offsets along the cuts.

The average extinction in the nucleus of NGC 4826 can also be estimated from the $^{12}\text{CO}(1-0)$ integrated intensity map of Fig. 4. Assuming a CO-to- H_2 conversion factor $X = N(\text{H}_2)/I_{\text{CO}} = 2.2 \times 10^{20} \text{ cm}^{-2} \text{ K}^{-1} \text{ km}^{-1} \text{ s}$ (Solomon & Barrett 1991) and the widely used gas-to-dust ratio of $N(\text{H}_2)/A_V = 1.0 \times 10^{21} \text{ cm}^{-2} \text{ mag}^{-1}$ (Bohlin et al. 1978), we obtain a mean $A_V \sim 10$ mag within the $42''$ 1–0 primary beam. This value is a factor of 6 higher than that derived from $B - I$ color. However, for several reasons the CO-based A_V value likely overestimates the dust column density that can absorb efficiently the stellar light. First, when this comparison is made, we implicitly assume a screen geometry for the H_2 slab with unit filling factor. Second, there is evidence that the CO-to- H_2 column density ratio X in central regions of galaxies may be lower than the standard Galactic value (see García-Burillo et al. 2000 and references therein). The extinction ‘discrepancy’ is even more severe at small scales. Fig. 14 compares the extinction map, estimated from $B - I$, with the CO maps. Confirming the impression given in Fig. 13, it is evident that molecular gas column density is not tightly correlated with the $B - I$ -based A_V (see also Block et al. 1994 and Sakamoto et al. 1999). Moreover, the clumpy structure of the interstellar medium makes difficult any

comparison between A_V values derived using data taken at very different spatial resolutions.

4.3. The star formation rate

We have measured the $\text{Pa}\alpha$ flux within the entire NICMOS field-of-view for NGC 4826, summing $> 3\sigma$ above sky, and found $F(\text{Pa}\alpha) = 7.4 \times 10^{-13} \text{ erg/s/cm}^2$. This gives a luminosity $L(\text{Pa}\alpha) = 1.5 \times 10^{39} \text{ erg/s}$, or a massive star formation rate (SFR) of $0.14 M_\odot/\text{yr}$, after correcting for a mean extinction A_V of 1.5 mag (this work). This is slightly lower than, although comparable to, the SFR of $0.22 M_\odot/\text{yr}$ estimated by Braun et al. (1994) from an $\text{H}\alpha$ image with a larger field-of-view. While this indicates rather vigorous star formation activity, it is much lower than in true nuclear starburst galaxies such as M 82, which have SFRs more than 10–50 times higher (O’Connell et al. 1995).

The number of ionizing photons can also be measured from the ionized gas emission, and from this we can derive the number of equivalent O stars necessary to ionize the gas. Using the coefficients given in Osterbrock (1989), we find that the total $\text{Pa}\alpha$ luminosity (not corrected for extinction) corresponds to 9.3×10^{51} ionizing photons. Taking an O7V star as representative, and assuming the number of Lyman continuum photons from

such a star to be 1×10^{49} (Leitherer 1990), this corresponds to roughly 930 O7V stars. Our estimates of ionizing photons are consistent with those of Pierini et al. (2002), if we consider the total area of the Pa α image compared to that of their spectroscopic slit. Because extinction may be an issue here, it is important to compare the number of ionizing photons derived from Pa α to that derived by Turner & Ho (1994) from the radio continuum. They find a factor of 3 fewer ionizing photons, but 20 times more massive stars, differences which almost certainly are due to the different normalizations. As noted by Turner & Ho (1994), the HII regions in NGC 4826 are one order of magnitude more energetic than the largest star-forming complexes in the Milky Way. In any case, the rough agreement between the estimates obtained from Pa α and from radio continuum maps is an independent confirmation that Pa α suffers from virtually no extinction (see also discussion in Sect. 4.2).

4.4. Star formation and compact star clusters in NGC 4826

The comparison of the Pa α morphology with that of the F450W and the $B - I$ color map reveals an interesting feature. The very blue compact source that emerges in the color cut at $17''$ lies within a ridge of HII regions or compact star clusters, visible in Fig. 13 just inside the edge of the “Evil Eye”. Surprisingly, this ridge of star formation does not coincide with the ionized gas emission ridge seen in Pa α (Fig. 11). The Pa α ridge is positioned roughly $4''$ closer (80 pc) to the nucleus than the arc of clusters, while the (very blue) $17''$ feature seems to contain little if any ionized gas. This result is consistent with the radial variations of ionized gas emission along the slit of Pierini et al. (2002), who found the peak of the ionizing photon flux at $\sim 14 - 15''$; at $17''$ the ionizing flux is approximately 30% of its peak value. These authors also found the hardness of the ionizing ratio to vary radially, with an abrupt softening at $17''$, roughly the same location where we find the blue compact source in the color cuts.

To better understand the pattern of star formation in NGC 4826, we have measured F450W and F814W magnitudes and (FWHM) diameters of compact sources in the ridge just inside the edge of the dust lane (see extranuclear cross in Fig. 13). All of the 25 sources measured appear to be star clusters, since their absolute F814W $\sim I$ magnitudes range from -7.4 to -8.9 (without correction for extinction) and their FWHMs from 4 to 29 pc. If we convert to V assuming $B - V \sim 0.7$ and correct for 1.5 mag of visual extinction, we find that the absolute V magnitudes (-8.5 to -9.9) are consistent with those of Super Star Clusters (SSCs) if they are old enough (in which case the correction to the fiducial age of 10 Myr would be > 1 mag).

If we infer the ages of these clusters from their $B - I$ color, which ranges from 0.65 to 2, we would derive a minimum age of 40 Myr (Leitherer et al. 1999) in the absence

of reddening. This would imply a minimum luminosity correction of ~ 1.5 mag (Whitmore et al. 1997), which would bring the luminosity of most of these compact star clusters into the SSC range of $M_V < -10.5$ at a fiducial age of 10 Myr (Billet et al. 2002). These clusters are not extremely compact, although this also could be related to an older age. In any case, the clusters must be older than 10 Myr, given the conspicuous absence of ionized gas emission in their immediate vicinity. The formation scenario for compact star clusters or SSCs, although not completely understood, appears to involve mergers (Bekki & Couch 2001) and/or high-pressure environments (e.g., Billet et al. 2002).

The ionized and the molecular gas profiles along the minor axis of NGC 4826 share a common feature: the disks are abruptly truncated beyond a ridge of old (> 10 Myr) compact star clusters. This pattern suggests a parallel pattern in the age of the star formation in the disk. Apparently stars are still vigorously forming elsewhere inside $R \sim 700$ pc where there is a significant molecular gas reservoir.

5. Counter-rotation and $m=1$ modes

NGC 4826 is a prototype among the large variety of counter-rotating disk galaxies. Counter-rotation can be purely stellar, involving stars versus gas, or characterized by the co-existence of two decoupled gas disks as seen in NGC 4826 (see compilations by Bertola & Corsini 1999, and Bettoni et al. 2001). The existence of counter-rotating components in disks suggests the active role that interactions, minor mergers and mass accretion processes may have in driving the evolution of galaxies. In hierarchical merging scenarios which explain how galaxy disks are built up, counter-rotating galaxies may naturally result from merger and/or accretion events. Partly due to the small number of observations, the prevalence of decoupled components in disk galaxies may have been underestimated thus far. Nevertheless, it is important to investigate which are the main gravitational instabilities induced by counter-rotation, and to analyze their influence on the removal of angular momentum from the gas. Analytical studies by Lovelace et al. (1997) indicate that the main dynamical instabilities linked with two-stream flows in galactic disks are one-arm spirals, i.e., $m=1$ modes.

García-Burillo et al. (1998, 2000) mapped at high-resolution the massive counter-rotating molecular disks of the spirals NGC 3593 and NGC 3626, searching for the signatures of counter-rotating instabilities. The maps of both galaxies show compact molecular gas disks with mixtures of $m=1$ and $m=2$ perturbations. With the help of self-consistent numerical simulations adapted for NGC 3593, García-Burillo et al. (2000) studied the development of disk instabilities. In their study, they found that counter-rotation drives rapidly evolving perturbations. The disk first develops stationary ($\Omega_p \sim 0$ km s $^{-1}$ kpc $^{-1}$) waves, leading with respect to the gas flow, followed later by a mixture of $m=1$ and $m=2$ slow (trailing) waves. The

nature of the instabilities is seen to depend critically on the assumed halo/disk mass ratio (see also Comins et al. 1997). Similarly to the aforementioned cases, NGC 4826 has a very compact molecular disk with signatures of $m=1$ perturbations at various scales. Rix et al. (1995) analyzed the stellar velocity distributions and estimated that a sizable fraction (10%–30%) of the stars in NGC 4826’s inner disk (radii $<50''$) could be in counter-rotation. This decoupled component could drive the two-stream flow instabilities we actually observe in the molecular disk. However, the reported fraction of counter-rotating stars is still compatible with the high-velocity dispersion of this kinematically hot region, and thus cannot be taken as firm evidence for counter-rotation in the stellar component.

In summary, the only *true* counter-rotating component in NGC 4826 may be the outer HI disk. The instabilities observed in the inner molecular disk are therefore not linked with counter-rotation: $m=1$ perturbations are detected in a region where two-stream flow is not detected. Additional evidence for this comes from the analysis of streaming motions made in the frame of density wave models (see Sect. 3.3.2). The CND lopsided instability and Arm I behave as fast modes, i.e., if the inner $m=1$ perturbations are wave modes they seem to have developed outside corotation. This contrasts with the low pattern speeds of $m=1$ modes which are known to be generated by the two-stream flow instability (Lovell et al. 1997; Comins et al. 1997; García-Burillo et al. 2000).

6. Gravitational instabilities and AGN fueling

6.1. Gravitational torques in NGC 4826

The objective of this section is to study if gravitational torques, derived from a fair representation of the stellar potential in the inner disk of NGC 4826, can account for the gas kinematics derived from CO. Furthermore, we examine the efficiency of gravitational torques exerted on the gas in the context of AGN fueling.

NIR maps can be used to derive the distribution of old stars as they are less affected by dust extinction or by stellar population biases. Here we have used a high-resolution near-infrared image of NGC 4826 taken with HST-NICMOS to derive the stellar potential within the inner 1 kpc of the disk. The HST field-of-view on NGC 4826 is 1024 pc and is sampled with a grid of 256x256 pixels of $0.203''$ spatial resolution. The image of the galaxy was completed along the 3rd vertical dimension by assuming an isothermal plane with a scale height constant with radius; this scale height is equal to 1/12th of the radial scale-length, i.e., ~ 160 pc. The gravitational potential is derived by a Fourier transform method on the grid from the NIR image. We also assumed a constant mass-to-light (M/L) ratio; the value of M/L is obtained by fitting the observed rotation curve.

The potential is decomposed as

$$\Phi(R, \theta) = \Phi_0(R) + \sum_m \Phi_m(R) \cos(m\theta - \phi_m) \quad (1)$$

we define the strength of the m -Fourier component, $Q_m(R) = m\Phi_m/R|F_0(R)|$ and its global strength over the disk as $\max_R Q_m(R)$ (e. g. Combes & Sanders 1981).

The strength of the total potential or maximal torque over the whole disk is defined by

$$Q_T(R) = \frac{F_T^{max}(R)}{F_0(R)} = \frac{\frac{1}{R} \left(\frac{\partial \Phi(R, \theta)}{\partial \theta} \right)_{max}}{\frac{d\Phi_0(R)}{dR}} \quad (2)$$

where $F_T^{max}(R)$ represents the maximum amplitude of the tangential force and $F_0(R)$ is the mean axisymmetric radial force, inferred from the $m=0$ component of the gravitational potential.

The strengths of the main m components for $R < 520$ pc are plotted in Fig. 15, together with the radial-variation of the corresponding phases, ϕ_m . It is interesting to notice that $m=1$ components are stronger than $m=2$ components in the stellar potential inside this region, especially for $R < 50$ pc. This indicates that there are also asymmetrical perturbations in the stellar disk.

Once the potential is obtained all over the grid, we deduce the forces (F_x and F_y) by derivation in each pixel, and can compute the average torque exerted on the gas. The surface density Σ of the gas is assumed proportional to the CO emission, either $^{12}\text{CO}(1-0)$ or $^{12}\text{CO}(2-1)$ (both maps are used). We resample the CO maps at the same pixel size of $0.203''$, and deproject them with the same geometrical angles as before. On each pixel, the torque T is computed by:

$$T = \Sigma(x.F_y - y.F_x)$$

We then compute the average over each radius of the torque per unit mass, i.e.:

$$t(R) = \frac{\int_R \Sigma(x.F_y - y.F_x)}{\int_R \Sigma}$$

The mean torques calculated using the $^{12}\text{CO}(1-0)$ map are plotted in Fig. 15, in units of $(km/s)^2$. The results based on the $^{12}\text{CO}(1-0)$ and $^{12}\text{CO}(2-1)$ maps are consistent. Most remarkably, oscillations between negative and positive values for $t(R)$ are roughly consistent with the diagnostic based on the change of sign of streaming motions for Arm I (related to a fast trailing wave, hence causing angular momentum gain) and Arm II (related to a slow trailing wave, hence causing angular momentum loss) (see Sect. 3.3.2). The corresponding stellar torques in the CND are marginally positive very close to the AGN ($R < 50$ pc), suggesting that stellar perturbations contribute little to AGN feeding. Again, this fits ‘qualitatively’ the streaming motions measured in CO, which would rather suggest outflow to some degree. The stellar torques change to negative values in the outer boundary of the CND; this roughly agrees also with the CO-based diagnostic.

While the radial variation of the stellar torques seem to account qualitatively for the changing signature of streaming motions, the maximum value of the mean torque is exceedingly small, however: $\sim 50(km/s)^2$. This implies that

the typical time-scale for the gas to lose its angular momentum for $R \sim 200$ pc is of about 1 Gyr. This is much longer than the gas dynamical time-scale at this radius (of the order of 2 Myr). Gravitational torques exerted on the gas due to the stellar potential are 'globally' quite weak. Weighted by the density, the total torque inside the evaluated region of the disk ($R \sim 520$ pc) is only marginally negative: the combination of all stellar perturbations seems to make the gas lose its angular momentum rather inefficiently.

We can ask whether our conclusions might be partly biased by the existence of residual extinction in the H -band image originally used to derive the gravitational potential. However, several arguments can be advanced suggesting that this bias is negligible. Although we estimate that extinction in the H band can locally reach $A_H \sim 0.20 - 0.25$ magnitudes in the northern dust lane arc (at $R \sim 250 - 300$ pc), this value is comfortably low elsewhere. In particular, we do not expect that the stellar gravitational potential is severely biased inside the CND, i.e., at the scales which are critical for evaluating the influence of gravitational torques on the AGN feeding. The derived values for $t(R)$ inside the CND (at $R < 80$ pc where $A_H < 0.02 - 0.03$), as well as in Arm I (developing on the southern side, where $A_H < 0.01$), are mostly weighted by the contribution of regions that are virtually extinction-free (see Fig. 14).

To estimate quantitatively the global influence of extinction on the derived torques, we have corrected the NIR map by a factor $\exp(\tau_H)$, where $\tau_H = 0.14A_V$ and A_V corresponds to the extinction map of Fig. 14. Confirming our expectations, the Fourier analysis of the gravitational potential thus derived is only slightly modified, and the average torques on the gas are practically unchanged. Although a detailed evaluation of residual extinction on the H -band image would require the use of several high-resolution optical and infrared images in order to resolve the age-extinction degeneracy (to be addressed in a forthcoming publication), we can conclude that the value derived here for $t(R)$ in the center of NGC 4826 is a robust estimate.

6.2. Gas self-gravity

Stellar perturbations are weak in the inner disk of NGC 4826 (except in the very center of the galaxy: $R \leq 50$ pc). Furthermore, we have found indications that they are probably inefficient to drive AGN fueling at $R \leq 520$ pc. Alternatively, self-gravitating gas instabilities may have a potential role in AGN feeding. When self-gravity of stars and/or gas is strong, galaxy disks are prone to gravitational instabilities. The local stability criterion, first established by Toomre (1964), ensures stability against axisymmetric perturbations in a stellar/gaseous galaxy disk when the column density of stars/gas ($N_{*,g}$) is smaller than a critical value ($N_{*,g}^{crit} = \kappa \sigma_v / \pi G$), i.e., when the so-called Toomre parameter $Q_{*,g} = N_{*,g} / N_{*,g}^{crit} > 1$.

Here, κ is the epicyclic frequency, σ_v is the velocity dispersion and G is the gravitational constant. Stability against non-axisymmetric perturbations, such as spirals and bars, is guaranteed when Q is significantly larger than 2.

The stability criterion for a realistic galaxy disk needs to take into account the strong coupling between the stellar and gaseous components through self-regulation and feedback (Combes 2001). Nevertheless, as a first step, it is useful to evaluate Q *separately* for the gas disk. In the particular case of AGN host disks, previous extinction maps derived from HST color images seem to indicate that non self-gravitating gas instabilities ($Q \sim 10-100$) may be ubiquitous in the inner 100-200 pc of Seyfert galaxies (Martini & Pogge 1999) and potential drivers of AGN fueling through energy dissipation in shocks and turbulent motions. This scenario can be fully tested by exploiting the information provided by ^{12}CO maps. Under certain assumptions, the ^{12}CO intensity gives a fair estimate of N_g . Moreover, the ^{12}CO kinematics can be used to derive Ω , κ , and σ_v in the disk. Hence, the derivation of Q maps follows straightforwardly.

Fig. 16 shows the variation of Q in the molecular disk of NGC 4826 as derived from $^{12}\text{CO}(1-0)$. Fig. 16 displays also a zoomed-in view of the Q map for the inner disk obtained from $^{12}\text{CO}(2-1)$. Gas column densities N_g are derived from 1-0 data as explained in Sect. 3.2.1. We have used the 2-1/1-0 line ratio maps discussed in Sect. 3.4 to calculate N_g from $^{12}\text{CO}(2-1)$. Ω and κ are derived from v_{rot} using standard definitions. Finally, σ_v has been estimated from CO second moment maps. The contribution to σ_v of the rotation curve gradient within the lobe(s) is found to be significant for $r < 2''$, but negligible elsewhere. The velocity dispersion is fairly constant in NGC 4826's disk and close to 10 km s^{-1} except for $r < 2''$, where σ_v doubles its value on average. In the following analysis we take for simplicity $\sigma_v = 10 \text{ km s}^{-1}$.

With these assumptions, Fig. 16 indicates that Arms I and II are self-gravitating perturbations: the two one-arm spirals are characterized by low Q values, ranging from 1 to 2. There are also indications for the CND lopsided instability to be self-gravitating ($Q < 2-3$), unless an unrealistic boost in velocity dispersion (not observed) or a much lower CO-to- H_2 conversion factor is invoked for $r < 2''$. NGC 4826 seems to be a good counterexample to the scenario suggested by Martini & Pogge 1999: the $m=1$ instabilities identified in NGC 4826 have low Q values. This suggests that self-gravity of the gas cannot be neglected and probably plays an essential role in the maintenance of the $m=1$ -type perturbations described in NGC 4826.

7. Summary and conclusions

We summarize the main results obtained here as follows:

- High-resolution ^{12}CO observations of NGC 4826 show that the bulk of its molecular gas lies in a highly structured disk of $M_{gas} \sim 3.1 \times 10^8 M_\odot$ which ends abruptly

- at $R \sim 700$ pc. The gas disk shows a preponderance of asymmetric perturbations ($m=1$ instabilities). There is a lopsided nuclear disk of 40 pc radius and two one-arm trailing spirals, which develop at different radii in the disk (Arm I: 200–350 pc, Arm II: 350–700 pc).
- The star formation pattern in the disk of NGC 4826 is strongly asymmetrical. The scales of the observed asymmetries resemble those of the various $m=1$ perturbations revealed in the disk of molecular gas. Furthermore, the star-forming ionized/molecular gas disk is truncated beyond a ridge of compact star clusters identified at $R \sim 700$ pc. This suggests an evolutionary trend for star formation in the disk of NGC 4826. Apparently massive star formation has ceased beyond $R \sim 700$ pc, but is still vigorously occurring inside this radius, fed by the significant molecular gas reservoir.
 - Gas kinematics reveal streaming motions related to the $m=1$ perturbations. A first analysis of these perturbations suggests that the inner $m=1$ instabilities may be fast trailing waves which have developed between corotation and an Outer Lindblad Resonance (OLR). This would imply that the AGN is probably not being generously fueled in the current epoch. An estimate of the radial variation of the mean gravitational torques due to the stellar potential confirms independently that stellar perturbations are inefficient to drive AGN fueling.
 - Arms I and II are both self-gravitating perturbations characterized by low values of the Toomre Q parameter ($Q=1-2$). There are also indications that the CNL lopsided instability is self-gravitating ($Q < 2-3$).

The two-stream flow instabilities, expected in counter-rotators, cannot explain the ubiquity of $m=1$ perturbations in the inner disk of the *Evil Eye*. Mechanisms other than counter-rotation have been suggested to trigger $m=1$ instabilities, such as interactions with companions (Weinberg 1994; Lovelace et al. 1999), central potentials dominated by massive black holes (Miller & Smith 1992; Taga & Iye 1998; Bacon et al. 2001) and response to an asymmetric halo (Jog 1997). Although pure $m=1$ modes are uncommon in galaxy disks, kinematic lopsidedness has been reported in 50% of spirals (Richter & Sancisi 1994). The self-consistent numerical simulations made by Junqueira & Combes (1996) showed that above a threshold central gas concentration, a typical galaxy disk (including stars and gas) is prone to develop one-arm (trailing) spiral perturbations. The strongest $m=1$ modes in their models appear between their corotation and their OLRs; in other words, these perturbations are fast. Fast $m=1$ trailing modes are decoupled from outer disk perturbations which only have 1/10 the speed of the inner waves. According to Junqueira & Combes (1996), the fast $m=1$ modes might reflect the action of the modal amplification mechanism described by Shu et al. (1990). The modes are excited by a slight off-centering of the stars and gas in the galaxy nucleus and develop mainly in the gas disk between

corotation and OLR. In summary, the inner $m=1$ perturbations identified in the gas disk of NGC 4826 could be tentatively explained by this scenario if the pattern speed of the perturbation is tuned to high enough values. As shown in Fig. 17, a value of $\Omega_p \geq 1500 \text{ km s}^{-1} \text{ kpc}^{-1}$ would push corotation well inside the disk, accounting for the spatial extent of Arm I in NGC 4826.

7.1. A possible scenario for the evolution of the inner kiloparsec of NGC 4826

While it appears that counter-rotation is not driving $m=1$ modes in the inner 1.5 kpc disk of NGC 4826 at present, a past gas accretion episode must be invoked to explain the decoupling of HI in the outer disk. Furthermore, the formation of compact/truncated star forming disks in counter-rotators, such as the one we see in NGC 4826, could represent the final stage of a process involving large-scale collisions between the accreted gas and the primary gas of the accretor (Rubin 1994, Thakar et al 1997, García-Burillo et al 2000). In general, the two components may have opposite angular momenta, implying substantial dissipation when they mix and, eventually, transformation from atomic to molecular phase in shocks. Large amounts of gas may fall towards the nucleus and form a circum-nuclear gas disk, whose final size will depend on the ratio of initial angular momenta of the two components. In close agreement with this picture, the kinematics of ionized gas reveal an orderly infall of gas from $R=2$ kpc to 800 pc in NGC 4826 (Rubin 1994). Moreover, the measured [NII]/H α ratio is close to 1 in this transition region, strongly suggesting shock excitation (Rubin 1994). In the course of this process, massive star formation is triggered along the “ridge” and in the nuclear disk. The time-scale for gas infall may be short and similar to the dynamical time, i.e., $\sim 10^7-8$ yr. This estimate is consistent with the age of the stellar clusters inferred from their $B-I$ colors.

The stellar velocities measured in the nucleus of NGC 4826 also imply a recent large mass infall episode. Kormendy (1993) has discussed NGC 4826 as an example of an early-type spiral with an anomalously low stellar velocity dispersion for its bulge luminosity ($\sigma_v = 90 \pm 5 \text{ km s}^{-1}$, later confirmed by Rix et al 1995). The expected value of σ_v for NGC 4826 predicted by the Faber-Jackson relation would be $\sim 160 \text{ km s}^{-1}$. As argued by Kormendy (1993), this indicates that the central brightness is dominated by a cold disk component. The formation of this cold central disk, in contrast to standard hot bulges, might be related to secular evolutionary processes involving large mass accretion.

Once the gas has settled in the nuclear disk, normal secular evolution can proceed. The onset of $m=1$ instabilities of the type described in NGC 4826 may be a consequence of secular evolution in disks with large gas masses. Detailed numerical simulations to be presented in a forthcoming paper (García-Burillo et al. 2003 in prep) will study the onset and evolution of asymmetric modes for

a case similar to NGC 4826, where the role of self-gravity of the gas may be essential.

Acknowledgements. We acknowledge the IRAM staff from the Plateau de Bure and from Grenoble for carrying out the observations and help provided during the data reduction. This paper has been partially funded by the Spanish MCyT under projects DGES/AYA2000-927, ESP2001-4519-PE and ESP2002-01693, and European FEDER funds.

References

- Bacon R., Emsellem E., Combes F., Copin Y., Monnet G., & Martin P. 2001, *A&A*, 371, 409
- Bekki, K., & Couch, W. J. 2001, *ApJ*, 557, L19
- Bertola, F., & Corsini, E. M. 1999 in *Proceedings of IAU Symposium 186: Galaxy Interactions at Low and High Redshift*, ed. J. E. Barnes, & D. B. Sanders, 149
- Bettoni, D., Galletta, G., García-Burillo, S., & Rodríguez-Franco, A. 2001, *A&A*, 374, 421
- Billett, O. H., Hunter, D. A., & Elmegreen, B. G. 2002, *AJ*, 123, 1454
- Block, D. L., Witt, A. N., Grosbol, P., Stockton, A., & Moneti, A. 1994, *A&A*, 288, 383
- Bohlin, R. C., Savage, B. D., & Drake, J. F. 1978, *ApJ*, 224, 132
- Böker, T., Calzetti, D., Sparks, W., Axon, D., Bergeron, L. E. et al. 1999, *ApJS*, 124, 95
- Braine, J., Combes, F., Casoli, F. et al 1993, *A&AS*, 97, 887
- Braun, R., Walterbos, R. A. M., & Kennicutt, R. C. 1992, *Nature*, 360, 442
- Braun, R., Walterbos, R. A. M., Kennicutt, R. C., & Tacconi, L. J. 1994, *ApJ*, 420, 558
- Buta R., & Combes F. 1996, *Fundamental of Cosmic Physics*, 17, 95
- Casoli, F., & Gerin, M. 1993, *A&A*, 279, L41
- Casoli, F., Dickey, J., Kazes, I. et al. 1996, *A&AS*, 116, 193
- Combes, F. 1988, in *Galactic and Extragalactic Star Formation*, ed. R.E. Pudritz & M. Fich, Kluwer, 475
- Combes, F. 2001, in *World Scientific, Advanced Lectures on the Starburst-AGN Connection*, ed. by I. Aretxaga, D. Kunth, & R. Mújica, 223
- Comins, N. F., Lovelace, R. V. E., Zeltwanger, T., & Shorey, P. 1997, *ApJ*, 484, L33
- de Jong, R. S. 1996, *A&A*, 313, 377
- Elmegreen, B. G., Elmegreen, D. M., Brinks, E. et al. 1998, *ApJ*, 503, L119
- Englmaier, P., & Shlosman, I. 2000, *ApJ*, 528, 677
- Friedli, D., & Martinet, L. 1993, *A&A*, 277, 27
- García-Burillo, S., Guélin, M., Cernicharo, J. 1993, *A&A*, 274, 123
- García-Burillo, S., Sempere, M. J., & Bettoni, D. 1998, *ApJ*, 502, 235
- García-Burillo, S., Sempere, M. J., Combes, F., Hunt, L. K., & Neri, R. 2000, *A&A*, 363, 869
- García-Burillo, S., Combes, F., Eckart, A. et al. 2003, in *ASP Conf. Ser., Active Galactic Nuclei: from Central Engine to Host Galaxy*, ed. S. Collin, F. Combes, & I. Shlosman, 423.
- Guilloteau, S., Delannoy, J., Downes, D. et al. 1992, *A&A*, 262, 624
- Guilloteau, S., & Lucas, R. 2000, in *ASP Conf. Ser.: Imaging at Radio through Submillimeter Wavelengths*, ed. J. G. Mangum & S. J. E. Radford, vol. 299
- Heckman, T. M., Smith, E. P., Baum, S. A. et al. 1986, *ApJ*, 311, 526
- Heckman, T. M., Blitz, L., Wilson, A. S., Armus, L., & Miley, G. K. 1989, *ApJ*, 342, 735
- Helfer, T. T., & Blitz, L. 1997, *ApJ*, 478, 162
- Helfer, T. T., Thornley, M. D., Regan, M. W. et al. 2003, *ApJS*, in press
- Heller, C. H., Shlosman, I. 1994, *ApJ*, 424, 84
- Ho, L. C., Filippenko, A. V., & Sargent, W. L. W. 1997, *ApJS*, 112, 315
- Holtzman, J. A., Burrows, C. J., Casertano, S., Hester, J., Trauger, J. T., Watson, A. M., & Worthey, G. 1995, *PASP*, 107, 1065
- Jog, C. J. 1997, *ApJ*, 488, 642
- Jogee, S., Baker, A. J., Sakamoto, S., Scoville, N. Z., & Kenney, J. D. P. 2001, in *ASP Conf. Ser., The Central Kiloparsec of Starbursts and AGN*, ed. by J. H. Knapen, J. E. Beckman, I. Shlosman, & T. J. Mahoney, vol. 249, 612
- Junqueira, S., & Combes, F. 1996, *A&A*, 312, 703
- Kenney, J.D., & Young, J.S. 1988, *ApJS*, 66, 261
- Kormendy, J. in *Proceedings of IAU Symposium 153: Galactic Bulges*, ed. H. Dejonghe & H. J. Habing 1993, 209
- Kormendy, J., & Bender R. 1999, *ApJ*, 522, 772
- Leitherer, C. 1990, *ApJS*, 73, 1
- Leitherer, C., Schaerer, D., Goldader, J. D. et al. 1999, *ApJS*, 123, 3
- Lequeux, J. 1983, *A&A*, 125, 394
- Lovelace, R. V. E., Jore, K. P., & Haynes, M. P. 1997, *ApJ*, 475, 83
- Lovelace, R. V. E., Zhang, L., Kornreich, D. A., & Haynes, M. P. 1999, *ApJ*, 524, 634
- Martini, P., & Pogge, R. W. 1999, *AJ*, 118, 2646
- Miller, R. H., & Smith, B. F. 1992, *ApJ*, 393, 508
- O'Connell, R. W., Gallagher, J. S. III, Hunter, D. A., & Colley, W. N. 1995, *ApJ*, 446, L1
- Osterbrock, D. W. 1989, *Astrophysics of Gaseous Nebulae and Active Galactic Nuclei*, University Science Books, Mill Valley, CA (USA)
- Pierini, D., Majeed, A., Boroson, T. A., & Witt, A. N. 2002, *ApJ*, 569, 184
- Piner, B. G., Stone, J. M., & Teuben, P. J. 1995, *ApJ*, 449, 508
- Pringle, J. 1996, *MNRAS*, 281, 357
- Regan, M. W., & Mulchaey, J. S. 1999, *AJ*, 117, 2676
- Regan, M. W., Thornley, M. D., Helfer, T. T., et al. 2001, *ApJ*, 561, 218
- Richter, O.-G., & Sancisi, R. 1994, *A&A*, 290, L9
- Rix, H.-W. R., Kennicutt, R. C., Braun, R., & Walterbos, R. A. M. 1995, *ApJ*, 438, 155
- Rubin, V. 1994, *AJ*, 107, 173
- Sakamoto, K., Okumura, S. K., Ishizuki, S., & Scoville, N. Z. 1999, *ApJS*, 124, 403
- Schinnerer, E., Eckart, A., & Tacconi, L. J. 2000a, *ApJ*, 533, 826
- Schinnerer, E., Eckart, A., Tacconi, L. J. et al. 2000b, *ApJ*, 533, 850
- Shlosman, I., Frank, J., & Begelman, M. C. 1989, *Nature*, 338, 45
- Shu, F. H., Milione, V., & Roberts, W. W. Jr. 1973, *ApJ*, 183, 819
- Shu, F. H., Tremaine, S., Adams, F. C., & Ruden, S. P. 1990, *ApJ*, 358, 49

- Solomon, P. M., & Barrett, J. W. 1991, in Proceedings of the 146th Symposium of the IAU, Dynamics of Galaxies and Their Molecular Cloud Distributions, ed. F. Combes & F. Casoli (Kluwer Academic Publishers, Dordrecht), 235
- Taga, M., & Iye, M. 1998, MNRAS, 299, 111
- Thakar, A. R., Ryden, B. S., Jore, K. P., & Broeils, A. H. 1997, ApJ, 479, 702
- Toomre, A. 1964, ApJ, 139, 1217
- Tully, B. 1988, Nearby Galaxies Catalog (Cambridge University Press, Cambridge and New York)
- Turner, J. L., & Ho, P. T. P. 1994, ApJ, 421, 122
- Vila-Vilaró, B., Taniguchi, Y., & Nakai, N. 1998, AJ, 116, 1553
- Walterbos, R. A. M., Braun, R., & Kennicutt, R. C. 1994, ApJ, 107, 184
- Weinberg, M. D. 1994, ApJ, 421, 481
- Whitmore, B. C., Miller, B. W., Schweizer, F., & Fall, S. M. 1997, AJ, 114, 1797
- Witt, A. N., Lindell, R. S., Block, D. L., & Evans, R. 1994, ApJ, 427, 227
- Young, J. S., Xie, S., Tacconi, L. et al. 1995, ApJS, 98,219

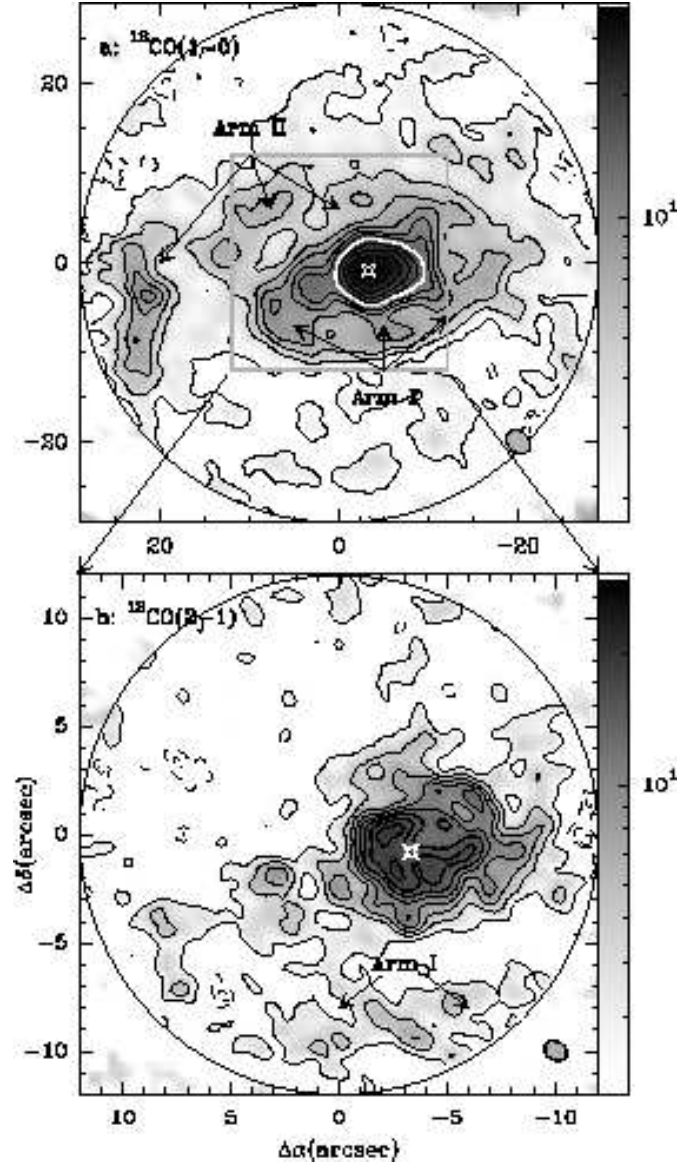


Fig. 4. a) $^{12}\text{CO}(1-0)$ integrated intensity contours in the inner $\sim 58''$ of NGC 4826. Contours beyond the displayed field-of-view have been screened as S/N ratio is lower than 3 for $r > 29''$. $\Delta\alpha$ and $\Delta\delta$ are offsets (in arcsec) with respect to the phase tracking center. Contours are -1.75, -0.88, 1.75, 4, 6, 8, 10, 12, 15, 18, 22 to 34 in steps of $5 \text{ Jy km s}^{-1} \text{ beam}^{-1}$. The dynamical center is indicated by the star marker. The white contour highlights the nuclear region here defined as CND. $1-\sigma$ noise = $0.25 \text{ Jy km s}^{-1} \text{ beam}^{-1}$ at the center of the image ($1-\sigma$ noise = $0.90 \text{ Jy km s}^{-1} \text{ beam}^{-1}$ at the edge of the displayed field-of-view) b) same as a) but for the $^{12}\text{CO}(2-1)$ line. The zoomed view shows emission coming from the inner $24''$. Contours beyond the displayed field-of-view have been screened as S/N ratio is lower than 3 for $r > 12''$. Contours are -2.4 -1.4 2.4 to 19.4 in steps of $2.4 \text{ Jy km s}^{-1} \text{ beam}^{-1}$. Thick contours inside the CND highlight the asymmetrical pattern. $1-\sigma$ noise = $0.36 \text{ Jy km s}^{-1} \text{ beam}^{-1}$ ($1-\sigma$ noise = $0.8 \text{ Jy km s}^{-1} \text{ beam}^{-1}$ at the edge of the displayed field-of-view). Positions of Arm I and II are indicated. Beam-sizes are represented by filled ellipses.

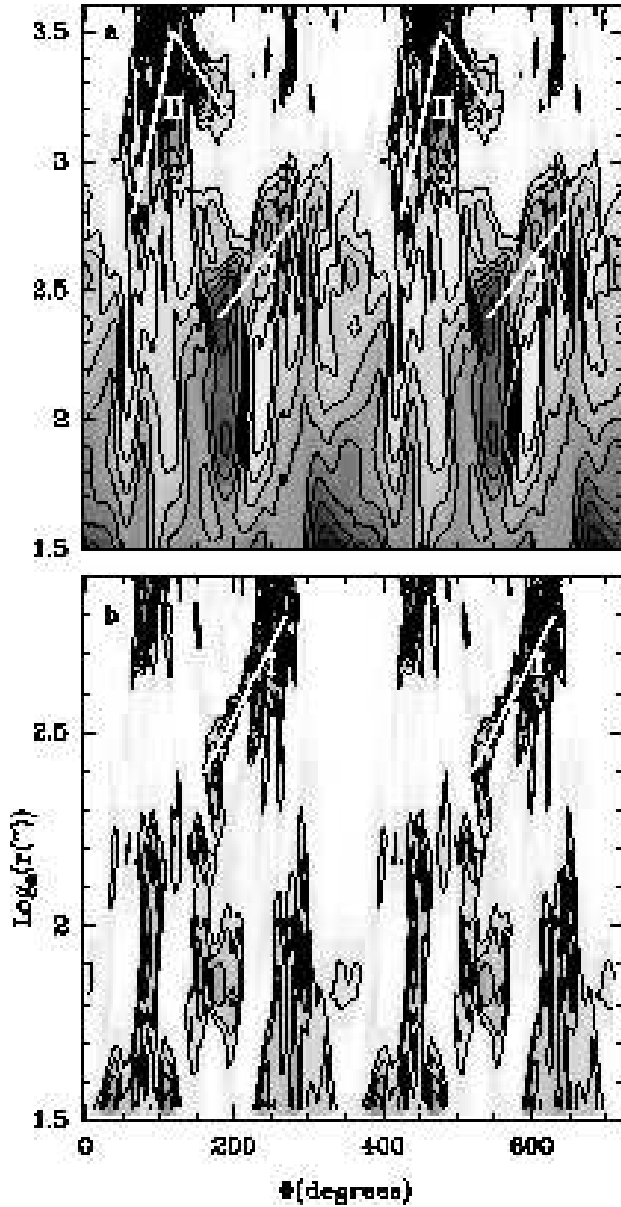


Fig. 5. **a)** Peak brightness $^{12}\text{CO}(1-0)$ map deprojected into the galaxy plane in $\text{Log}_e(r)-\Phi$, where r (in arcsec) and Φ (in degrees) are the polar coordinates. Variable r is the galaxy deprojected radius in " relative to the dynamical center and Φ is the azimuthal angle in degrees, measured counter-clockwise from the western side of the major axis. We assume an inclination of $i=60^\circ$ and position angle $PA=112^\circ$ for the NGC 4826 disk (see Sect. 3.3.1). The locations of the two $m=1$ spirals (Arms I and II), appearing as two straight ridges, are high-lighted by the white-shaded lines. **b)** Same as **a)** but for the $^{12}\text{CO}(2-1)$ line. Arm I and the beginning of Arm II are detected.

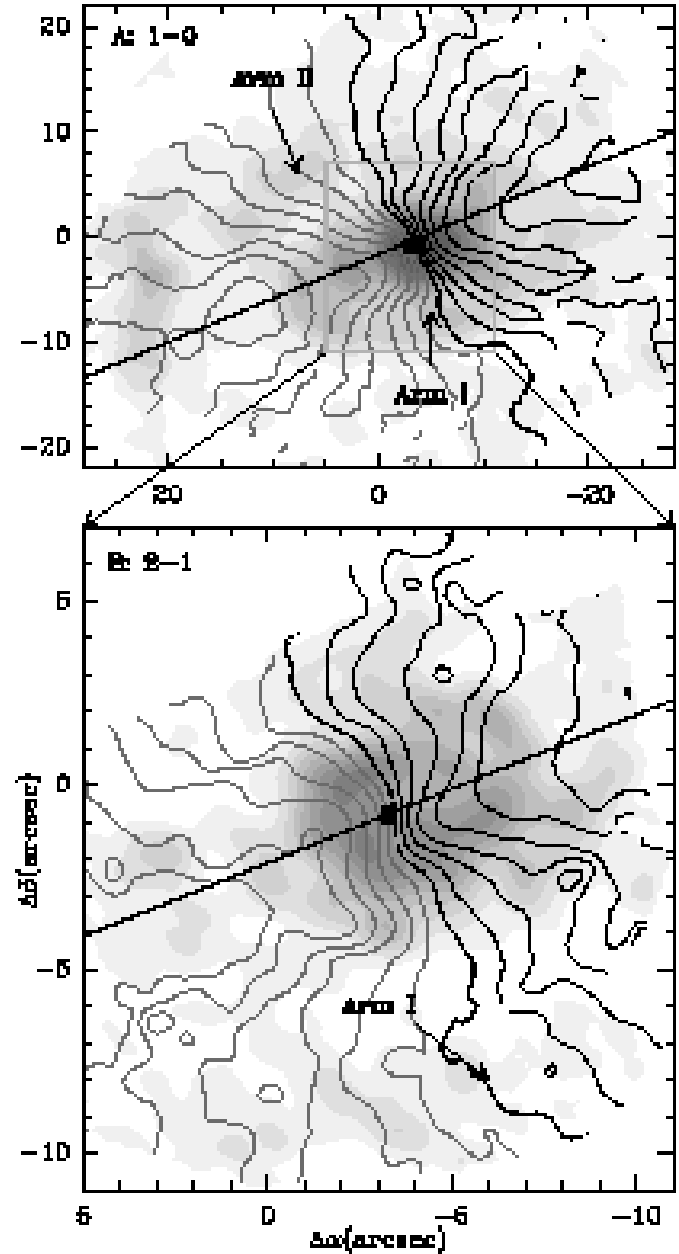


Fig. 6. **a)** Overlay of the mean-velocity field derived from the 1-0 data, in line contours, spanning the range $(-160 \text{ km s}^{-1}, 160 \text{ km s}^{-1})$ in steps of 20 km s^{-1} on the integrated intensity map of $^{12}\text{CO}(1-0)$. Integrated intensity as in Fig. 4 starting by $1.75 \text{ Jy km s}^{-1} \text{ beam}^{-1}$. Velocities are here referred to $v_{sys}(LSR)=416 \text{ km s}^{-1}$ (thick contour). Solid black (grey) lines are used for positive (negative) velocities. The straight line at $PA=112^\circ$ indicates the position of NGC 4826's major axis. The star marks the AGN position. **b)** Same as **a)** but for the $^{12}\text{CO}(2-1)$ line. Integrated intensity contours as in Fig. 4 starting by $2.4 \text{ Jy km s}^{-1} \text{ beam}^{-1}$. Velocities span the range $(-120 \text{ km s}^{-1}, 120 \text{ km s}^{-1})$ in steps of 20 km s^{-1} .

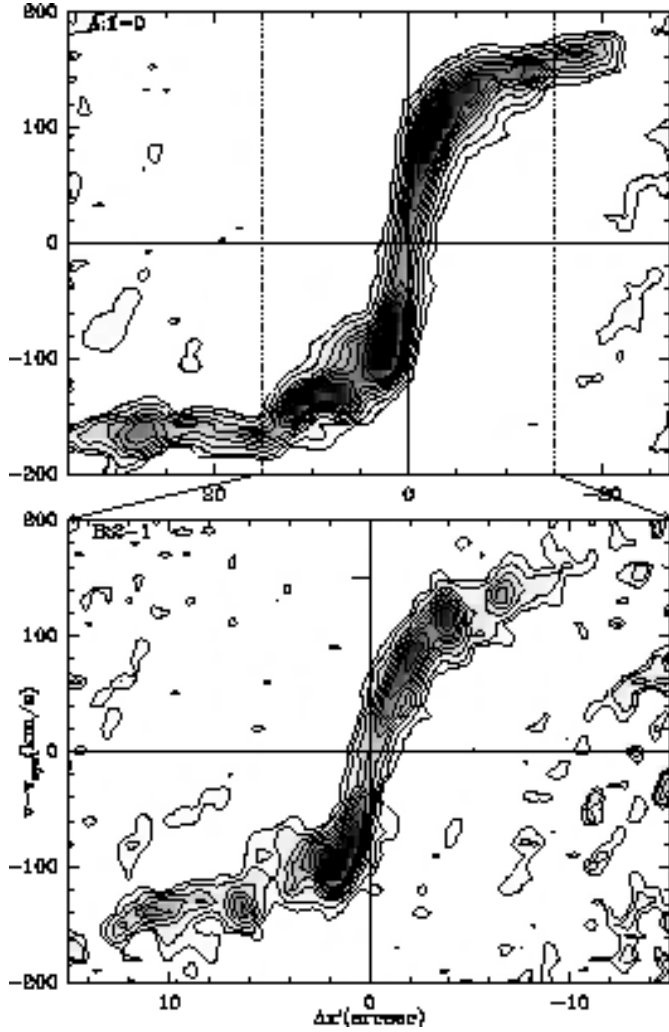


Fig. 7. **a)** We show the $^{12}\text{CO}(1-0)$ position-velocity (p-v) diagram along the major axis of NGC 4826 (line contours and grey scale range: 0.015, 0.035 to $0.27 \text{ Jy beam}^{-1}$ in steps of $0.035 \text{ Jy beam}^{-1}$). Velocities have been re-scaled to $v_{\text{sys}}^{\text{LSR}} = 416 \text{ km s}^{-1}$ and x' offsets are relative to the dynamical center. **b)**: Same as **a)** but for the $^{12}\text{CO}(2-1)$ line in the inner $r \sim 15''$. Contours are the same as in **a)**.

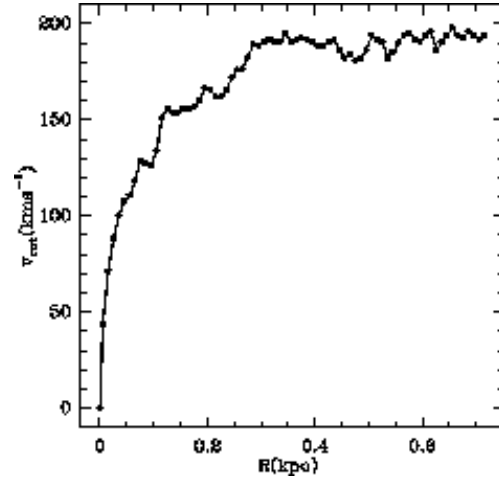


Fig. 8. Rotation curve obtained from the combined 1–0 + 2–1 CO data in NGC 4826 to a radius of $R=700 \text{ pc}$.

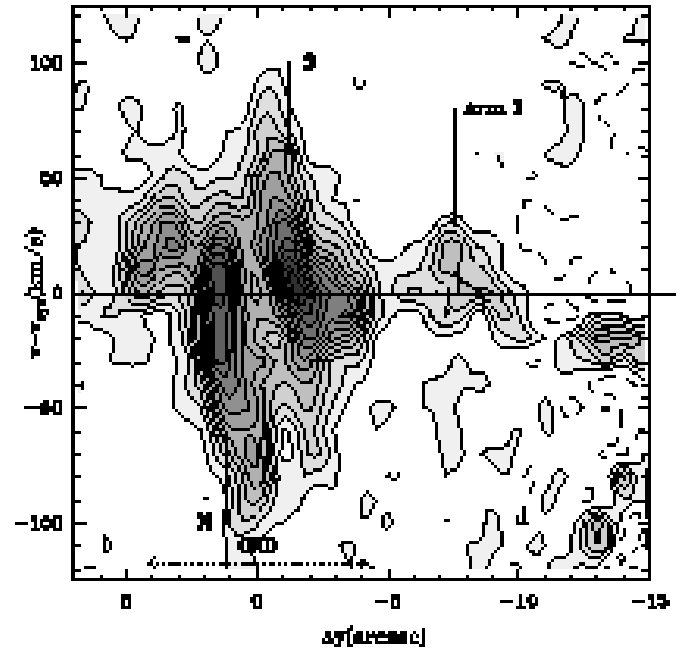


Fig. 9. $^{12}\text{CO}(2-1)$ position-velocity plot taken along the NGC 4826's minor axis. We indicate the position of Arm I, and the N/S crossings of the CND lopsided instability. The gas kinematics show local signatures of outflow motions at these positions.

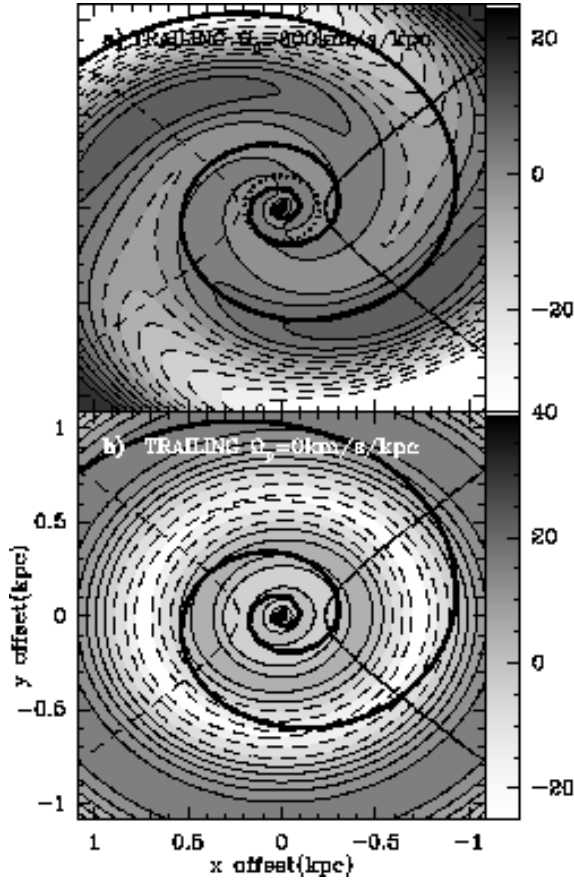


Fig. 10. We display the velocity perturbations of the gas flow, projected into the plane of the sky (v_{pert}), due to a *fast* ($\Omega_p=800 \text{ km s}^{-1}\text{kpc}^{-1}$) (a) and a *slow* ($\Omega_p=0 \text{ km s}^{-1}\text{kpc}^{-1}$) (b) $m=1$ trailing spiral wave. x and y axes are parallel to the major and minor galaxy axes ($x>0$ eastwards, $y>0$ northwards), and we assume $i=-30^\circ$ (i.e., northern side is closer to us). Thin line contours and gray scale range from -10 , -8 to 16 in steps of 2 km s^{-1} (dashed contours for negative values). Isovelocities $v=-80 \text{ km s}^{-1}$ (dashed line) and $v=80 \text{ km s}^{-1}$ (thick line) define the orientation of circular rotation in the disk (clockwise). The potential minimum locus is represented by the logarithmic spiral. The position of corotation is indicated by the dotted circle in the top panel.

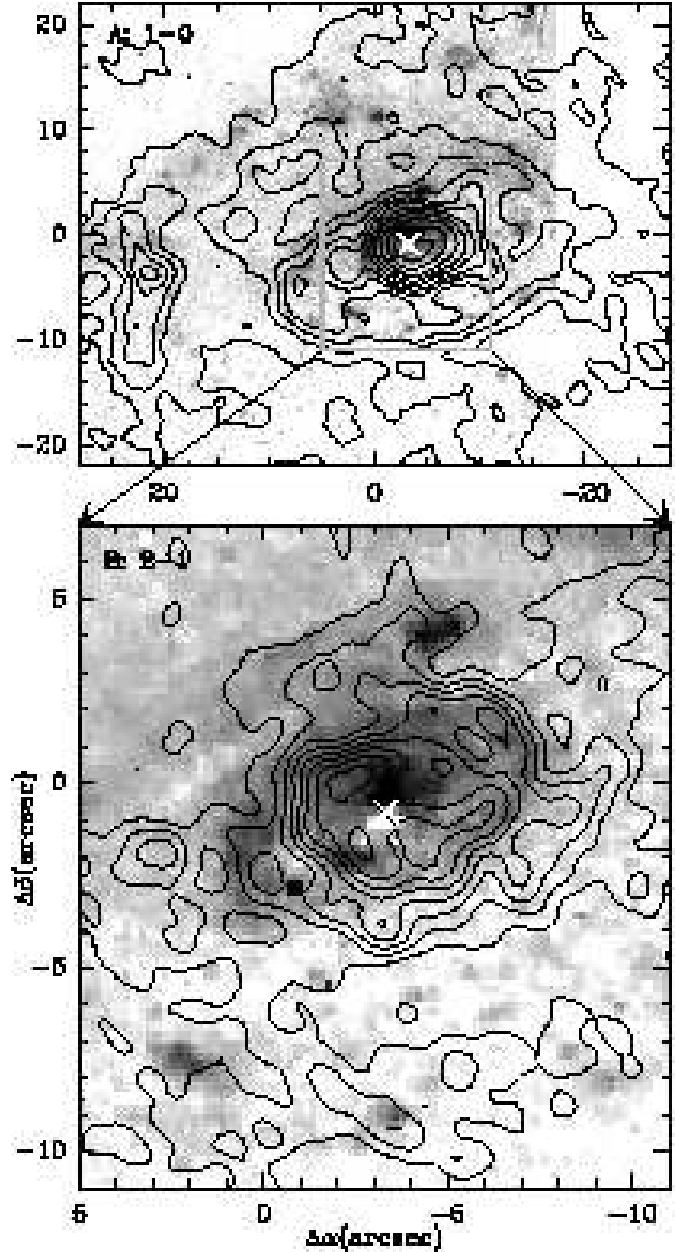


Fig. 11. We display the overlay of the $\text{Pa}\alpha$ integrated intensity image, derived from the HST F187N and F160W NICMOS filters (grey logarithmic scale ranges from $3.1 \cdot 10^{-12}$ – $2.1 \cdot 10^{-11} \text{ erg s}^{-1} \text{ cm}^{-2} \text{ pix}^{-1}$ in the top panel and from $7.7 \cdot 10^{-13}$ – $3.1 \cdot 10^{-11} \text{ erg s}^{-1} \text{ cm}^{-2} \text{ pix}^{-1}$ in the bottom panel; grey scale increases from light to dark), and the integrated intensity maps obtained for the 1–0 (top) and 2–1 (bottom) lines of ^{12}CO in the disk of NGC 4826 (same contours as Fig. 6).

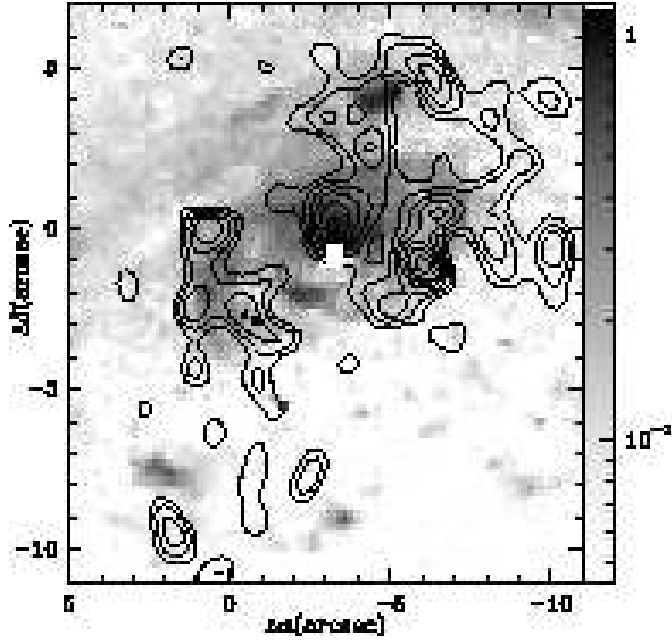


Fig. 12. The VLA radio-continuum map at 2cm (mostly thermal emission) taken from Turner and Ho (1994) (in contours from 35% to 95%, in steps of 10% of the maximum= 1 mJy beam^{-1}) is overlaid on the Pa α image of NGC 4826 (in grey scale, as shown). The lopsided star formation in the nucleus has a strong maximum offset by $\sim 16 \text{ pc}$ northward from the position of the AGN (marked with a square).

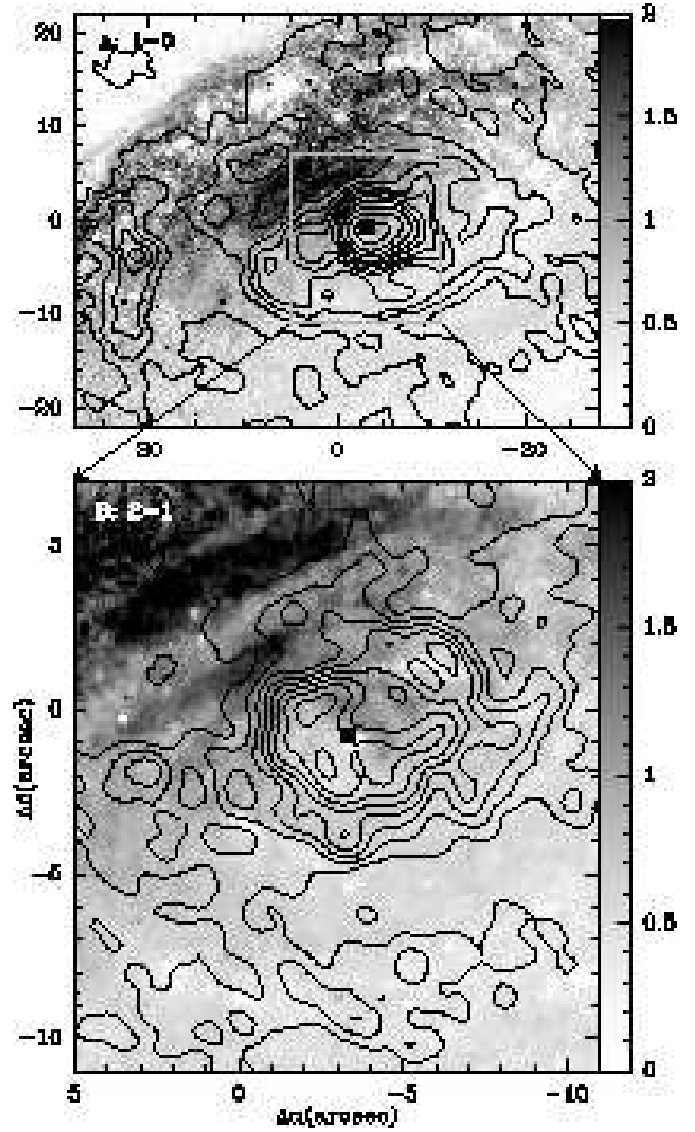


Fig. 14. Same CO contours as in Fig. 11 overlaid on extinction A_V derived from the HST broad-band $B-I$ color map. Greyscale ranges from $A_V=0$ to 2.

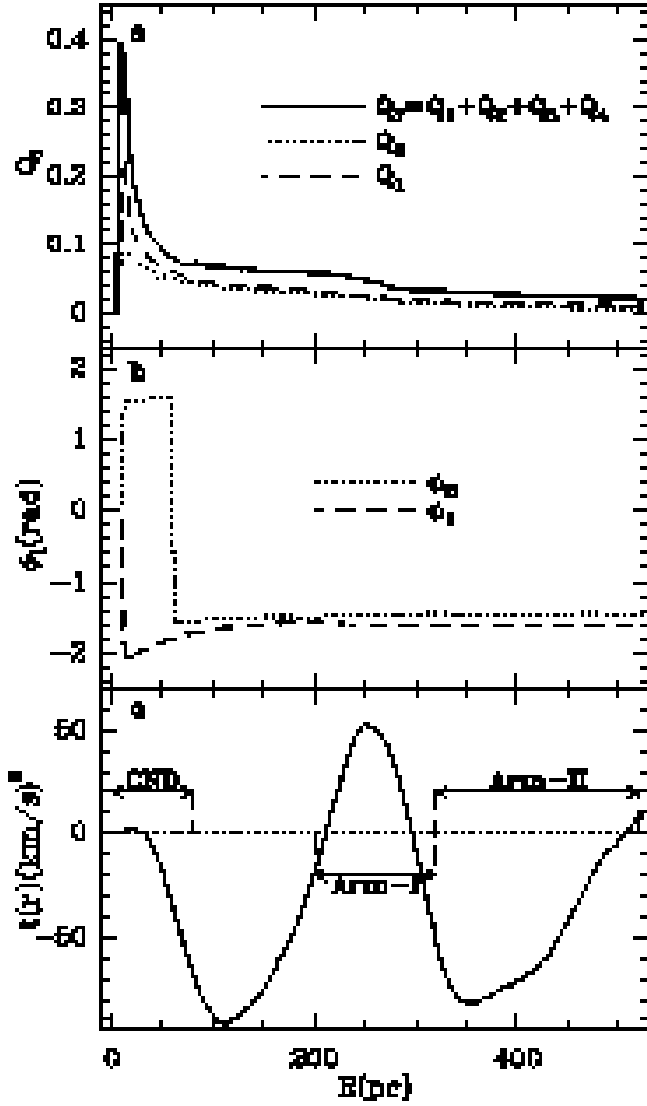


Fig. 15. **a(top)** Strength of the i -Fourier components of the stellar potential of NGC 4826 derived from the HST-NICMOS image of the galaxy nucleus. We represent the main components— Q_1 and Q_2 —and the sum Q_T . **b(middle)** The phases Φ_i of the potential components are plotted for $i=1,2$. **c(bottom)** Radial variation of the average torque— $t(R)$ —per unit mass. We indicate the radial extent of CND, Arm I and Arm II.

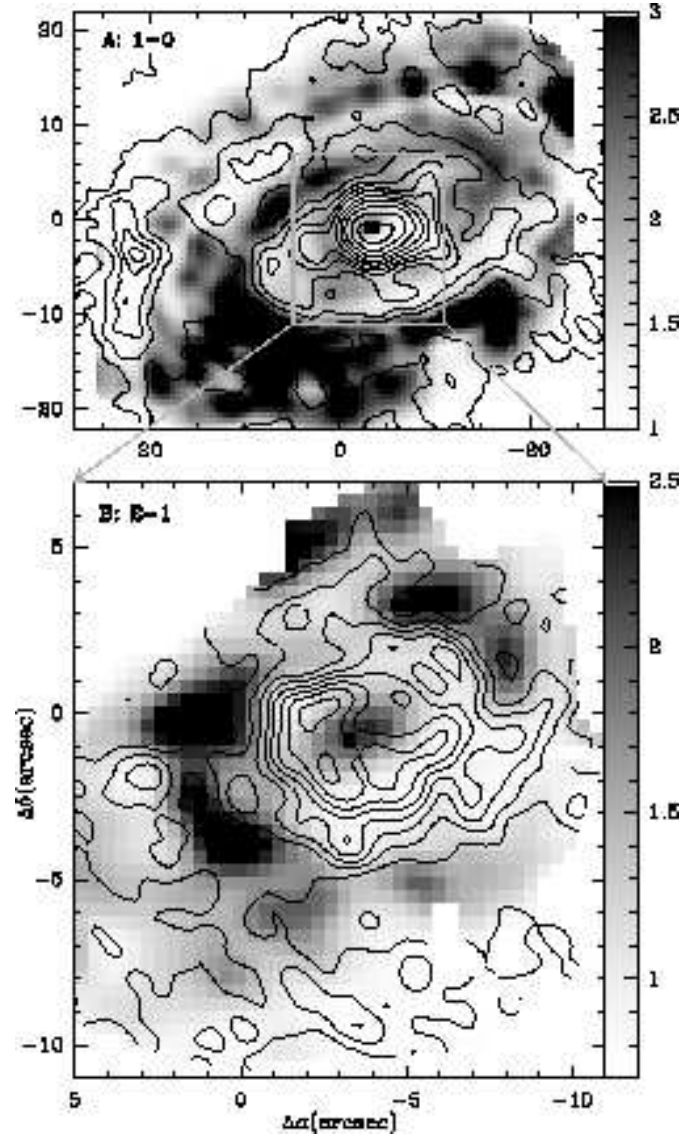


Fig. 16. Estimation of the order of magnitude of the Toomre Q parameter (grey scale ranges from 1–3 in the top panel and from 0.7–2.5 in the bottom panel) overlaid on the integrated intensity maps obtained for the 1–0 (top) and 2–1 (bottom) lines of ^{12}CO in the disk of NGC 4826 (same contours as Fig. 6).

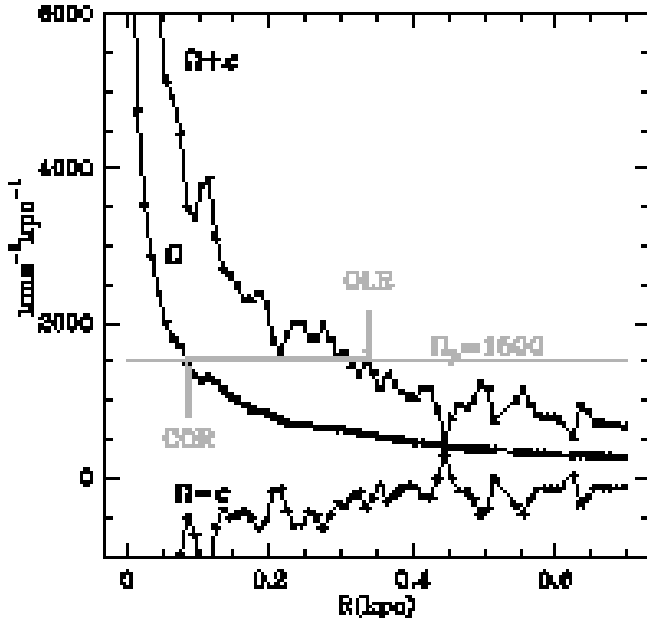


Fig. 17. The principal epicyclic frequencies Ω , $\Omega-\kappa$ and $\Omega+\kappa$ in the inner disk of NGC 4826. The pattern speed $\Omega_p=1500 \text{ km s}^{-1}\text{kpc}^{-1}$ has been purposely chosen to locate the inner $m=1$ mode of Arm I between its corotation and OLR.